

A Novel Multi-Dimensional Boltzmann Neutrino Transport Scheme for Core-Collapse Supernovae

Conrad Chan^{*} and Bernhard Müller[†]

School of Physics and Astronomy, Monash University, Clayton, Australia, VIC 3800

29 June 2020

ABSTRACT

We introduce a new discrete-ordinate scheme for solving the general relativistic Boltzmann transport equation in the context of core-collapse supernovae. Our algorithm avoids the need to spell out the complicated advection terms in energy and angle that arise when the transport equation is formulated in spherical polar coordinates, in the comoving frame, or in a general relativistic spacetime. We instead approach the problem by calculating the advection of neutrinos across momentum space using an intuitive particle-like approach that has excellent conservation properties and fully accounts for Lorentz boosts, general relativistic effects, and grid geometry terms. In order to avoid the need for a global implicit solution, time integration is performed using a locally implicit Lax-Wendroff scheme that correctly reproduces the diffusion limit. This will facilitate the use of our method on massively parallel distributed-memory architectures. We have verified the accuracy and stability of our scheme with a suite of test problems in spherical symmetry and axisymmetry. To demonstrate that the new algorithm works stably in core-collapse supernova simulations, we have coupled it to the general relativistic hydrodynamics code CoCoNuT and present a first demonstration run of a $20M_{\odot}$ progenitor with a reduced set of neutrino opacities.

Key words: methods: numerical — radiative transfer — neutrinos — supernovae: general

1 INTRODUCTION

Since Colgate & White (1966) proposed that neutrinos play a crucial role in reviving the stalled shock in core-collapse supernovae (CCSNe), numerical models have incorporated neutrino transport in some form, with varying degrees of sophistication. The neutrino transport problem in CCSNe poses one of the most computationally challenging problems to date. The extreme range in densities within the supernova results in optically thick regions in which neutrinos are diffusive, and optically thin regions in which neutrinos are decoupled from the fluid and can stream freely. The so-called “gain region” behind the stalled shock, which the success of the explosion hinges upon, lies within the semi-transparent region between the two regimes, where an accurate treatment of the neutrino distribution function is important (for modern reviews of the topic, see Mezzacappa 2005; Janka 2012; Burrows 2013). The most accurate treatment of neutrino transport calls for the solution of the full Boltzmann equation (Mihalas & Mihalas 1984),

$$\frac{\partial f}{\partial t} + \mathbf{u} \cdot \nabla f = C(f), \quad (1)$$

(shown here the Newtonian form for clarity) which describes

the neutrino momentum distribution f at every point in space (Figure 1). Evolving through time, this results in a 7-dimensional problem. The left-hand side of the equation is the advection equation, which couples together the spatial dimensions. The right-hand side contains the collision integral, which accounts for interactions between neutrinos and matter, and couple together the momentum space dimensions. Interaction rates are sensitive to the neutrino energy, necessitating an energy-dependent treatment. Additionally, there are three flavors of neutrinos (electron, muon, and tauon) and respective antineutrinos for a total of six species. Due to the different interaction rates of each species, their transport behaviour is considerably different, thus the core-collapse problem also calls for a flavour-dependent treatment. In general, even flavour can evolve via neutrino oscillations, a purely quantum mechanical effect (Wolfenstein 1978; Mikheyev & Smirnov 1985).

The first serious attempts to incorporate neutrino transport into core-collapse simulations relied on the flux-limited diffusion (FLD) scheme in spherical symmetry, one of the simplest approximations of radiation transport (Arnett & Truran 1970; Arnett 1977; Bowers & Wilson 1982; Bruenn 1985; Myra et al. 1987; Baron et al. 1989; Cooperstein & Baron 1992). FLD is still employed in several modern supernova codes as an economical approach to multi-dimensional transport (e.g. Walder et al. 2005; Bruenn et al. 2018; Rahman et al. 2019). This approximation solves the diffusion equation for mean intensity of radiation with the assumption that the angular distribution is isotropic, discarding directional dependence of

^{*} conrad.chan@monash.edu

[†] bernhard.mueller@monash.edu

the field (while in “multi-group” implementations still retaining energy dependence). In the limit of high optical depth, the diffusion approximation is the exact solution. At low optical depth where neutrinos stream freely, a flux-limiter is necessary to prevent advection above the maximum transport velocity (i.e. the speed of light). The semi-transparent region where shock revival is decided by neutrino heating, however, is handled using ad-hoc switching prescriptions. Since the choice of flux-limiter determines the flux-factor, which in turn affects the neutrino heating rate, this can lead to inaccurate results (Yamada et al. 1999; Burrows et al. 2000). Comparisons with more sophisticated schemes have shown that the FLD approximation smears out anisotropies in the radiation field (Ott et al. 2008). This is especially crucial in rotating models, which exhibit a large-scale asymmetry in the post-shock flow. Nonetheless, these approximations were necessary in the pioneering CCSN simulations due to the sheer computational infeasibility of solving the full Boltzmann equation at the time.

That is not to say that schemes to solve the full Boltzmann equation had not yet been devised. The discrete ordinate method (S_N) had already been developed by Carlson (1967) to solve the neutron transport problem in nuclear reactors, which was later adapted to supernova modelling (Yueh & Buchler 1977; Mezzacappa & Bruenn 1993c). The S_N method is a brute-force approach, directly discretising all of the variables of the Boltzmann equation, in particular the direction of radiation propagation. In practice, this is extremely computationally expensive, so the first CCSN simulations to apply this scheme were run in spherical symmetry, which reduced the dimensionality of the problem (Yamada et al. 1999; Mezzacappa et al. 2001; Liebendörfer et al. 2001, 2004).

Methods based on solving the moment equations derived from the Boltzmann equation (so called “moment methods”) have also been employed. In these methods, the individual directions of radiation are integrated over to obtain the moments of radiation, which become the variables of the Boltzmann equation. An arbitrary number of equations can be derived, though the solution of each equation requires the solution for a higher moment, thus requiring the system to be truncated at some point using an approximate closure relation obtained from the known moments. Truncating at the zeroth moment yields the diffusion approximation, while modern schemes are most commonly two-moment methods, solving for energy and momentum. The closure may be an algebraic relation (e.g. Minerbo 1978; Levermore 1984), as implemented by Pons et al. (2000); Just et al. (2015); O’Connor (2015); Kuroda et al. (2016); Roberts et al. (2016); Skinner et al. (2016, 2019). The use of an algebraic closure provides significant computational cost savings while still being sufficiently accurate in spherical symmetry (Richers et al. 2017). Alternatively, the closure can be obtained by solving a model Boltzmann equation using the moments in variable Eddington factor (VEF) methods (Rampp & Janka 2000; Burrows et al. 2000; Rampp & Janka 2002). Moment methods model the angular dependence of radiation while avoiding direct discretisation of the momentum space. Implementations that use a closure based on an exact solution of the Boltzmann equation are still considered as Boltzmann transport solvers.

As the field evolved to the understanding that multi-dimensional fluid flows are important in supernovae, there too became a demand for multi-dimensional neutrino transport solvers. Computational power, however, could not keep up, and compromises were made in most multi-dimensional simulations. Early attempts at multi-dimensional calculations discarded energy-dependence entirely (Herant et al. 1994; Burrows et al. 1995; Fryer & Heger 2000; Fryer & Warren 2004), though these “gray” sim-

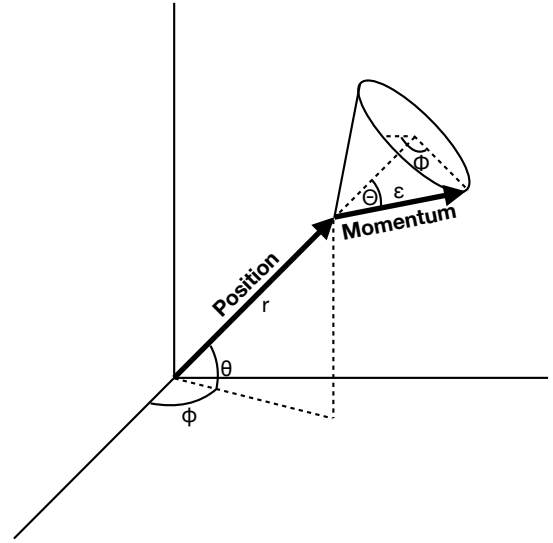


Figure 1. Illustration of the six-dimensional phase space. The coordinates r , θ , and ϕ specify the position of a neutrino, while Θ and Φ specify the direction of propagation, with ϵ specifying the energy (magnitude). The Θ angle is conventionally expressed as $\mu = \cos \Theta$, where $\mu \in [-1, 1]$.

ulations have since been shown to yield considerably different results compared their energy-dependent counterparts. Implicit finite differencing, which was employed in many spherically symmetric solutions, is expensive in two and three dimensions, so multi-group codes often resort to the “ray-by-ray” approximation and solves the transport problem in one dimension along angular rays and assuming the neutrino distribution to be axially symmetric around the radial direction (Buras et al. 2006). Others have continued to use the multi-group flux-limited diffusion approximation (Walder et al. 2005; Burrows et al. 2007; Swesty & Myra 2009; Rahman et al. 2019), which can also be combined with the ray-by-ray approximation (Bruenn et al. 2018). Meanwhile, truly multidimensional S_N schemes were developed (Livne et al. 2004; Sumiyoshi & Yamada 2012; Nagakura et al. 2014), although some omitting energy redistribution and velocity-dependent effects to avoid the implicit coupling across energy groups and similarly, true multidimensional moment schemes were also developed (Hubeny & Burrows 2007; Just et al. 2015; Kuroda et al. 2016; Roberts et al. 2016; Skinner et al. 2016, 2019).

There are a handful of other ambitious treatments that have been explored, for example, the P_N scheme of Radice et al. (2013) which decomposes the momentum space into spherical harmonics, and the spectral scheme of Peres et al. (2014) which decomposes real space using a Fourier basis and momentum space using a Chebyshev basis. These approaches, however, still remain in the demonstration phase and have not yet been used for full supernova simulations. As an alternative approach to solving the Boltzmann equation, the Monte Carlo (MC) method, in which the trajectories of a large sample of particles are directly evolved, solves the transport problem with full angular dependence (Fleck & Cummings 1971; Fleck & Canfield 1984). It has been applied in the context of CCSN simulations (Janka & Hillebrandt 1989; Janka 1992; Abdikamalov et al. 2012; Richers et al. 2017) and it has also been used to supplement the two-moment scheme by provid-

ing a closure (Foucart 2018). Though MC methods are accurate and scale excellently, they are generally noisy, requiring high resolution for a smooth solution. Recently, the particle-like moment closure method of Ryan & Dolence (2020) has demonstrated improved convergence compared to MC, though it is yet to be applied to neutrino transport.

To enable more affordable multi-dimensional simulations in the interim as we await for advancements in computing power, there has also been an interest in alternative efficient transport approximations in recent years. Liebendörfer et al. (2009) have made improvements to the diffusion approximation, and Müller & Janka (2015) have devised a fast approximation to the stationary transport equation using a combination of a two-stream solution of the Boltzmann equation and an algebraic Eddington factor to obtain closure.

Aside from limits in computing power, there are several challenges on the algorithm front. Most importantly, a numerical solution to the Boltzmann equation should be stable, while accurately reproducing the correct behaviour in the diffusion and free-streaming limit. These requirements have led to the proliferation of moment methods, which satisfy physical limits by construction, and are easier to discretise in a numerically stable way. Current schemes that solve the Boltzmann equation rely on a global implicit solution to ensure stability. A traditional explicit implementation has timesteps severely restricted by the Courant limit of neutrinos travelling at the speed of light, commonly an order of magnitude smaller than that of the fluid. Most problematically, the source terms on the right-hand-side of the equation are stiff and non-linear, necessitating an even smaller time-step for stability, which an implicit scheme circumvents.

The major downside of fully implicit schemes is that they necessitate an iterative solution that couples the entire grid, usually in real space *and* momentum space. Achieving good parallel scaling with this degree of coupling is difficult. While in spherical symmetry it is possible to fit the entire domain on a single processor, 2D and 3D simulations often span multiple computer nodes, usually decomposed based on the spatial grid. Since an implicit solution requires information from the entire grid at every timestep, inter-node communication becomes a bottleneck. While the ray-by-ray scheme circumvents this by implicitly solving the 1D solution along rays, this is not true multi-dimensional transport. While the ray-by-ray method may yield acceptable results in supernova simulations of non-rotating progenitors (Glas et al. 2019), errors may be significant in the presence of large-scale asymmetries in the radiation field, for example when dealing with rapidly rotating neutron stars, accretion disks, and jet outflows.

In this paper, we describe a three-dimensional S_N scheme to solve the Boltzmann equation in general relativity, implemented explicitly in real space to allow scalability but implicitly in momentum space to ensure stability. This explicit-implicit hybrid approach (Ascher et al. 1997) has been used in the context of neutrino transport by Radice et al. (2013); Just et al. (2015); Chu et al. (2019). The space-explicit implementation has the benefit of easier maintenance and the flexibility to be extended to cover additional physics, e.g. treating neutrino oscillations by solving the quantum kinetic equations (Sigl & Raffelt 1993; Cardall 2008; Volpe 2015; Richers et al. 2019). Although in an explicit scheme, timesteps are restricted by the Courant condition, the sound speed in the proto-NS interior is a significant fraction of the neutrino velocity (c), so the neutrino timesteps and fluid timesteps are not too dissimilar. We postulate that for large multi-dimensional simulations, the improved scaling of our scheme will make up for the additional cost of shorter

timesteps. An explicit scheme also opens up the possibility for variable time-stepping based on the local Courant limit, an optimisation that is practically impossible in an implicit scheme. We couple our scheme to the CoCoNuT hydrodynamics solver (Dimmelmeier et al. 2005; Müller et al. 2010) with the conformal flatness condition (CFC) for the spacetime (Isenberg 2008; Wilson et al. 1996; Cordero-Carrion et al. 2009). Just as the first solutions to the Boltzmann equation were developed well before they were affordable, the exascale computing power required to use our scheme in 3D is still in the distant horizon. We demonstrate the capabilities of our scheme in 1D and 2D, and argue that it will be equally applicable in future 3D simulations.

2 SOLUTION STRATEGY

2.1 A “derivative-free” approach

The left-hand side of the Boltzmann equation is simply an advection equation. It is preferred, however, to solve it in the comoving frame, since the collision terms on the right-hand side is naturally expressed in the comoving frame. The Lorentz transformation of the collision integral from the comoving frame to the lab frame is cumbersome, and achieving the correct diffusion limit in a lab-frame approach is non-trivial. These problems are somewhat mitigated in the mixed-frame approach where the lab frame opacities are expressed in terms of the comoving frame opacities by means of a first-order Taylor expansion, but this approach is inherently limited to $O(v/c)$ in accuracy. There is, however, a downside to the comoving frame approach, since it results in advection across the momentum dimensions of the phase space, in the form of energy and angle derivatives that can obscure the original meaning of the advection equation. In this section, we explain how these terms come about and propose a strategy for avoiding them.

For problems with spherical geometry, radiation typically transitions towards a radially-peaked distribution. On such a grid, a natural and commonly adopted momentum space coordinate is one that is aligned with the radial direction in real space. The complication, however, is that the direction of propagation with respect to the radial direction of a particle with a non-radial momentum component varies as it travels inwards or outwards. This manifests as a $\frac{\partial}{\partial \mu}$ derivative when the Boltzmann equation is expressed in the spherically symmetric form

$$\frac{1}{c} \frac{\partial f}{\partial t} + \mu \frac{\partial f}{\partial r} + \frac{1 - \mu^2}{r} \frac{\partial f}{\partial \mu} = \mathfrak{C}[f]. \quad (2)$$

When a moving background fluid is introduced, the Boltzmann equation becomes even more complicated in the comoving frame. As a particle moves from one cell to another, the neutrino energy and direction of propagation shifts, manifesting as the $\frac{\partial}{\partial \epsilon}$ term and an additional $\frac{\partial}{\partial \mu}$ term respectively, and an additional $\frac{\partial f}{\partial r}$ term due to the advection of neutrinos with the fluid, giving the $O(v/c)$ accurate equation

$$\begin{aligned} \frac{1}{c} \frac{\partial f}{\partial t} + (\mu + \beta) \frac{\partial f}{\partial r} + \frac{1 - \mu^2}{r} \frac{\partial f}{\partial \mu} + (1 - \mu^2) \left[\mu \left(\frac{\beta}{r} - \frac{\partial \beta}{\partial r} \right) - \frac{1}{c} \frac{\partial \beta}{\partial t} \right] \frac{\partial f}{\partial \mu} \\ + \mu \epsilon \left[\mu \left(\frac{\beta}{r} - \frac{\partial \beta}{\partial r} \right) - \frac{1}{c} \frac{\partial \beta}{\partial t} - \frac{1}{\mu r} \right] \frac{\partial f}{\partial \epsilon} = \mathfrak{C}[f] \end{aligned} \quad (3)$$

where $\beta = v/c$ (Mihalas & Mihalas 1984). Once a curved spacetime is included, the Boltzmann equation quickly becomes unwieldy, with the introduction of many additional derivatives that account

for gravitational ray-bending and redshift:

$$p^{\hat{\mu}} L_{\hat{\mu}}^{\mu} \frac{\partial f}{\partial x^{\mu}} - \Gamma^i_{\hat{\nu}\hat{\mu}} p^{\hat{\nu}} p^{\hat{\mu}} P^i_{\hat{\nu}} \frac{\partial f}{\partial p^{\hat{\nu}}} = \mathfrak{C}[f] \quad (4)$$

where the x^{μ} are the spacetime position coordinates in the lab frame, $p^{\hat{\nu}}$ are the momentum space coordinates in the comoving frame, $\Gamma^i_{\hat{\nu}\hat{\mu}}$ are the Christoffel symbols, $L_{\hat{\mu}}^{\mu}$ is the coordinate transformation from the lab frame to the comoving frame, and $P^i_{\hat{\nu}}$ is the transformation between curvilinear and cartesian momentum space coordinates (see [Cardall et al. 2013](#), for a derivation). To implement the equation into a numerical scheme, each of the terms have to be converted into a finite difference representation, with care required to maintain any desired conservation properties (e.g. the S_N scheme of [Liebendörfer et al. 2004](#)).

All of these derivatives, however, arise simply as a consequence of the change of basis in momentum space as a particle is transported from one cell to another and as the metric and velocity field evolve in time. One can eliminate some of the derivatives by expressing the equation in the lab frame, but the derivatives associated with the grid geometry will remain, and the collision term becomes much more complicated because the opacities need to be transformed.

Rather than implementing each derivative explicitly in the Boltzmann equation, we instead propose in our solution to transport neutrinos along characteristics (geodesics), handling the advection terms in the lab frame while keeping the distribution function in the lab frame. In their destination cell, advected neutrinos are mapped back to the momentum space grid in the comoving frame based on their comoving-frame four-velocity. This strategy is reminiscent of the semi-Lagrangian method for advection problems, only that the mapping of the advected solution is carried out in momentum space only.

We illustrate our idea in [Figure 2](#) by considering neutrinos streaming outwards through a fluid moving inwards with a typical shock velocity profile. Observers comoving with the shock will observe the neutrino energy to be blue-shifted. In traditional discretisations of the Boltzmann equation, this advection of neutrinos to a higher energy group is handled by the $\frac{\partial}{\partial \epsilon}$ derivative. We instead consider representing the advection of neutrinos in the lab frame, where the neutrino energy is constant but the energy groups in each cell are shifted relative to their neighbours. The key to our method is that the blue-shift in neutrino energy is accounted for by fluxes through these misaligned interfaces. No derivatives need to appear in our discretisation — they are instead handled automatically by the misalignment of cells. This procedure can also be applied to the transition of propagation angle to $\mu \rightarrow 1$ as neutrinos move outwards. In fact, it can be applied to any transformation between bases in momentum space. The remaining task is then to identify the appropriate transformation between the bases of each cell, or in terms of our illustration, to find the fluxes through the misaligned interfaces, so that a neutrino originating from one cell can be mapped into the basis of the destination cell in a conservative manner, which we explain in detail in [Section 3.2](#).

Another strategy to avoid derivatives in energy is to use different energy space grids in the lab frame and in the comoving frame [Nagakura et al. \(2014\)](#). In terms of implementation, our single (comoving) frame approach is in fact conceptually similar in that we also employ linear interpolation to map between adjacent frames. Where our scheme differs is that we map directly to the destination

frame, bypassing the intermediate lab frame.¹ Our implementation goes beyond this existing work by applying the remapping procedure generally, to not only the shifts in energy but also angle, arising from not only Lorentz boosts but also geometric rotations and general relativistic Hamiltonian “kicks”.

2.2 Treatment of relativistic effects

General relativistic (GR) effects become important in core-collapse supernovae after the formation of the neutron star, and indeed, most state-of-the-art models account for these effects either with GR transport ([Yamada et al. 1999](#); [Liebendörfer et al. 2004](#); [Müller et al. 2010](#); [Roberts et al. 2016](#); [Kuroda et al. 2016](#)), or with an approximate GR treatment using Newtonian pseudopotentials ([Rampp & Janka 2002](#); [Marek et al. 2006](#)). Our scheme has been developed with the intention of coupling to GR hydrodynamic codes. For simplicity, we restrict ourselves to the CFC case, but our scheme is readily generalised to GR simulations without this approximation.

When a neutrino moves in space and time, its lab-frame velocity components will be deflected according to the geodesic equation. The lab-frame velocity is calculated by first transforming the comoving-frame velocity into the Eulerian frame using the Lorentz boost, and then into the lab frame using the metric. After the deflection is calculated, the comoving-frame velocity in the destination cell is calculated by applying the frame transformations in reverse. The fluxes through cell interfaces ([Section 3.3](#)) are always calculated using the lab-frame velocities. The full chain of transformations from the source cell (src) to the destination cell (dst) is

$$\tilde{u}_{\text{src}} \xrightarrow{\Lambda_{\text{src}}} \hat{u}_{\text{src}} \xrightarrow{M_{\text{src}}} u_{\text{src}} \xrightarrow{G,K} u_{\text{dst}} \xrightarrow{M_{\text{dst}}^{-1}} \hat{u}_{\text{dst}} \xrightarrow{\Lambda_{\text{dst}}^{-1}} \tilde{u}_{\text{dst}}. \quad (5)$$

where \tilde{u} , \hat{u} , and u are the four-velocities in the comoving, Eulerian, and coordinate frame. The Lorentz transformation $\tilde{u} \leftrightarrow \hat{u}$ is described in [Section 3.2.2](#). The transformation $\hat{u} \leftrightarrow u$ and from the coordinate frame is described in [Section 3.2.3](#). The transformation $u_{\text{src}} \rightarrow u_{\text{dst}}$ accounting for the geometric rotation and Ricci rotation of velocity components between cells is described in [Sections 3.2.1 and 3.2.4](#). We show how each of these velocities are used in our scheme in [Figure \(3\)](#).

2.3 Reproducing the diffusion limit using a stable explicit scheme

A finite-difference scheme is convergent if and only if it is consistent with the original equation and it is stable. It is essential for any Boltzmann scheme to be able to reproduce the correct solution within all regimes encountered during core-collapse. While reproducing the advection equation in the optically thin limit is relatively trivial, the optically thick limit requires more care. In optically thick regions where the mean free path of a neutrino of order $\mathcal{O}(\text{cm})$ is much smaller than the zone width, the scheme should yield the correct diffusion limit, which even the most primitive flux-limited diffusion schemes achieve by construction. In principle, this challenge can be avoided by choosing a sufficiently fine grid spacing that resolves the mean free path of neutrinos, but in practice, it is exceedingly computationally expensive to do so. The more prudent

¹ The scheme of [Nagakura et al. \(2014\)](#) also differs in that it is *globally* implicit, coupling together space and momentum dimensions.

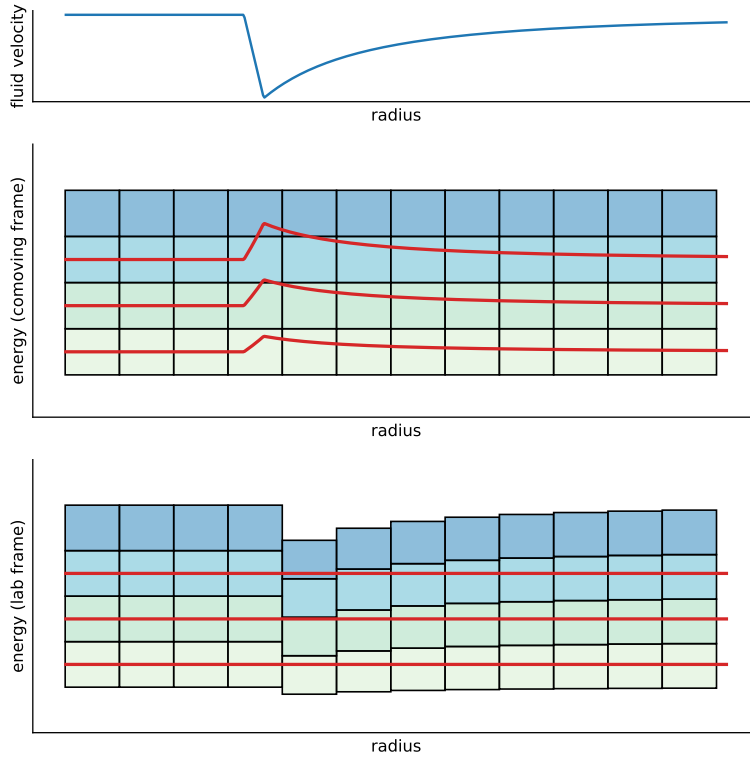


Figure 2. Illustration of the advection in energy space as a neutrino moves through the typical shock velocity profile (top), as viewed in the comoving frame (center) and the lab frame (bottom). Red curves indicate the characteristics of neutrinos through this slice of the phase space as they travel outwards. The shaded cells represent the finite-volume elements of the scheme.

solution is to use a differencing scheme that represents a valid discretisation of the diffusion equation.

The formulation of Carlson (1967) solves the problem by using a backward-time centered-space scheme, which is consistent with the diffusion limit. When Yueh & Buchler (1977) applied this scheme to the core-collapse problem, however, they found that oscillatory behaviour arises when the distribution is close to kinetic equilibrium or in the presence of steep gradients. To circumvent this, they instead adopt upwind differencing in space. Although stable, the step method generally produces incorrect fluxes in the diffusion limit (Iarsen & Morel 1989), so they introduce an artificial diffusion term. On the other hand, Mezzacappa & Bruenn (1993b) avoid the need for a diffusion term in their implementation by interpolating between centered differencing and upwind differencing (i.e. between first- and second-order differencing in space) to achieve consistency in optically thick regions and avoid oscillations in problematic regions.

To achieve stability, all of these schemes have used implicit backward-time differencing, which is unconditionally stable. Though this circumvents a restrictive $\Delta t \lesssim \frac{\kappa \Delta x^2}{c}$ limit (where κ is the opacity) on the timestep, an accurate solution in the regime where advection is dominant (i.e. the Péclet number $Pe \sim \kappa \Delta x$ is small) still requires timesteps that are not too much greater than the stability limit $\Delta t = \Delta x/c$ for explicit advection. Explicit implementa-

tions of high-resolution shock-capturing schemes are not suitable, usually because they are unstable. Any reconstruction steps that maintain stability will introduce jumps at interfaces, leading to numerical diffusion that disrupts convergence to the physical diffusion limit. In moment schemes, convergence to the diffusion limit is usually achieved by an ad-hoc treatment (Audit et al. 2002; González et al. 2007; O’Connor 2015). These approaches are not satisfactory for our purposes, since they require the diffusion limit to be known. In GR and when solving the more general quantum-kinetic equations, the diffusion limit is non-trivial.² It is desirable to avoid manual intervention if possible.

² Very few method papers for recent diffusion or two-moment codes for core-collapse supernovae actually address the issue of the correct diffusion limit in detail. (e.g. Rahman et al. 2019). However, in addition to including the correct metric factors when computing spatial and temporal derivatives, the correct diffusive flux in a (nearly) static GR space-time must be computed using spatial derivatives of the zeroth moment J at constant neutrino energy at infinity, not at constant comoving frame energy. The diffusive flux must therefore generally include an additional energy derivative of the zeroth-moment, unless an adapted energy grid in the comoving frame is used as in (Müller & Janka 2015; Bruenn et al. 2018). This is necessary to ensure that the diffusive flux establishes the correct thermal equilibrium $\alpha T = \text{const.}$ in a static space-time (e.g. Tolman & Ehrenfest 1930; Pons et al. 1999).

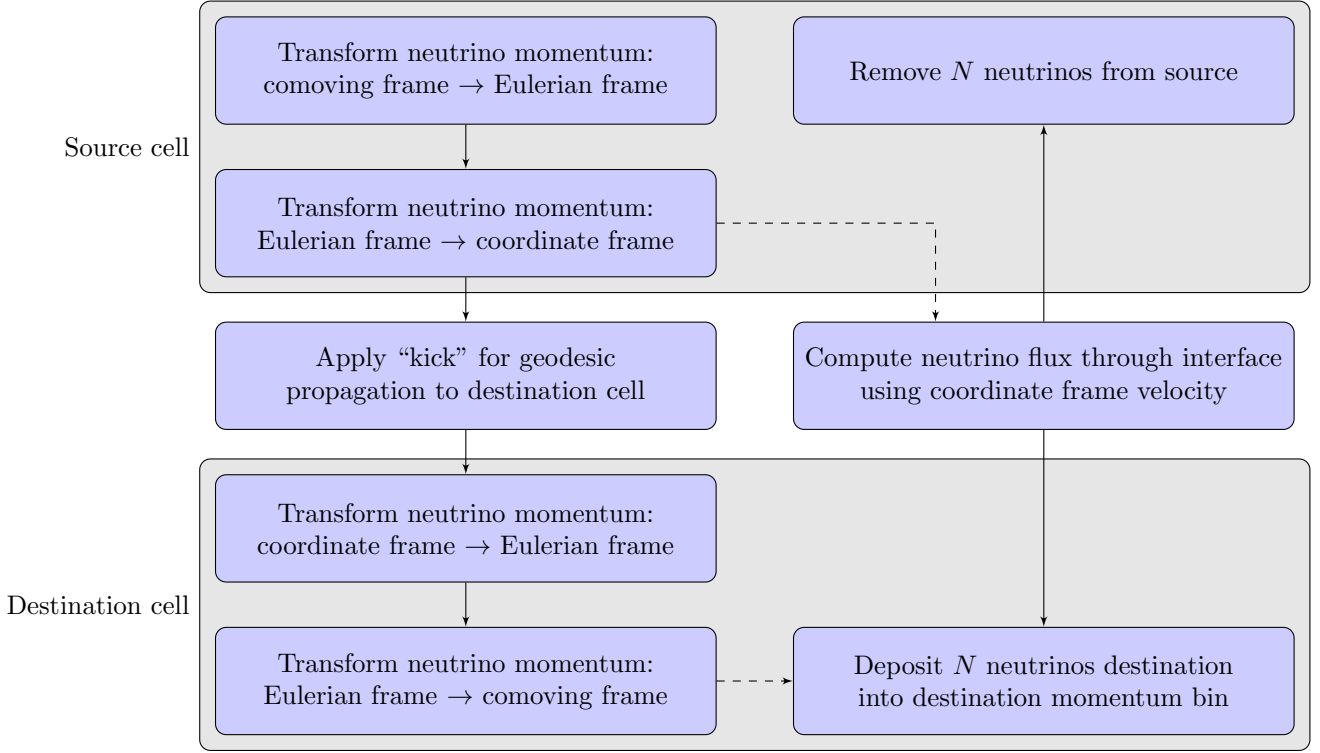


Figure 3. Flowchart of the chain of transformations from the source comoving frame to the destination comoving frame. The boxes on the right show how the upwind flux (Section 3.3.2) is computed. The fluxes are calculated in the coordinate frame, and the neutrinos are deposited into the destination comoving frame in the destination momentum bin obtained from the chain of transformations. The procedure for the Lax-Wendroff flux (Section 3.3.1) is conceptually the same if we treat the reconstructed interface distribution as the destination cell for the half-steps, and use the reconstructed coordinate-frame velocity for the flux computation in the full step.

We propose discretising using a locally-implicit (semi-explicit) Lax-Wendroff scheme, where the fluxes are computed using a half-timestep at the cell interfaces:

$$\frac{f_{a+\frac{1}{2}}^{n+\frac{1}{2}} - f_{a+\frac{1}{2}}^n}{\frac{1}{2}\Delta t} + u \cdot \frac{f_{a+1}^n - f_a^n}{\Delta x} = \mathcal{C} \left[f_{a+\frac{1}{2}} \right], \quad (6)$$

where $f_{a+\frac{1}{2}}^n = \frac{1}{2}(f_a^n + f_{a+1}^n)$. We show that this is consistent with the diffusion limit in Appendix A. The explicit time differencing of the advective fluxes has the advantage of avoiding a global coupling of the spatial grid, allowing computational scalability. The key to our approach is to use implicit time differencing for the collision terms at the half- and full-steps of the Lax-Wendroff scheme which allows the timestep Δt to be independent of opacity κ while coupling the grid only in momentum space. The Lax-Wendroff scheme is stable for the advection equation when the CFL limit is met, and the addition of a collision term will only further dampen the growth of errors. Similar to Mezzacappa & Bruenn (1993b), we avoid oscillatory behaviour in optically thin cells by interpolating between Lax-Wendroff fluxes and upwind fluxes.

3 IMPLEMENTATION

3.1 Discretisation

We exploit the spherical symmetries of CCSNe by adopting spherical polar spatial coordinates

$$x = r \sin \theta \cos \phi, \quad (7)$$

$$y = r \sin \theta \sin \phi, \quad (8)$$

$$z = r \cos \theta. \quad (9)$$

We discretise the six-dimensional phase space into finite volume elements. In real space, cell interfaces are defined as the surface on a plane bounded by the four line segments connecting four adjacent vertices of the grid. The vertices have coordinates

$$r_{a+\frac{1}{2}} \in [0, r_{\max}], \quad a = 0, \dots, N_r \quad (10)$$

$$\theta_{b+\frac{1}{2}} \in [\theta_{\min}, \theta_{\max}], \quad b = 0, \dots, N_\theta \quad (11)$$

$$\phi_{c+\frac{1}{2}} \in [\phi_{\min}, \phi_{\max}], \quad c = 0, \dots, N_\phi \quad (12)$$

where $r_{a+\frac{1}{2}}$ are spaced non-uniformly (arbitrary choice), and $\theta_{b+\frac{1}{2}}$ and $\phi_{c+\frac{1}{2}}$ are spaced uniformly.³ The area ΔA of the interface is defined as the area of the flat surface bounded by the quadrilateral formed by four adjacent vertices, and the volume ΔV of the

³ We use the “ $i + \frac{1}{2}$ ” notation to refer to the interface between cells i and $i + 1$.

cell is defined as the volume bounded by the hexahedron (frustum) formed by eight adjacent vertices.⁴

We also adopt spherical coordinates for the momentum space:

$$p_x = \epsilon \sin \Theta \cos \Phi, \quad (13)$$

$$p_y = \epsilon \sin \Theta \sin \Phi, \quad (14)$$

$$p_z = \epsilon \cos \Theta. \quad (15)$$

We use the definition $\mu = \cos \Theta$. At each point on the grid, the $\mu = 1$ momentum cell is aligned with the radial direction (Figure 1), to exploit the fact that the distribution transitions to radially-peaked at large radii. This means the momentum space vectors at two points with differing angular coordinates are not the same. We discretise the momentum vector into spherical shells bounded by the surfaces

$$\epsilon_{i+\frac{1}{2}} \in [\epsilon_{\min}, \epsilon_{\max}], i = 0, \dots, N_\epsilon \quad (16)$$

and solid angle elements $\Delta\Omega$ bounded by the coordinates

$$\mu_{j+\frac{1}{2}} \in [-1, 1], j = 0, \dots, N_\mu \quad (17)$$

$$\Phi_{k+\frac{1}{2}} \in [0, 2\pi], k = 0, \dots, N_\epsilon \quad (18)$$

where $\mu_{j+\frac{1}{2}}$ are spaced such that the cell volumes are the Gauss-Lobatto weights (Boyd 2000), and $\Phi_{k+\frac{1}{2}}$ are spaced uniformly.

In the comoving frame, neutrinos have four-velocity

$$u^\nu = (1, u^i), \quad (19)$$

where u^i is the three-velocity.⁵ Using our chosen momentum space coordinates, the velocity of a neutrino is given by the zenith coordinate μ and the azimuthal angle Φ , such that

$$u^\nu = (1, \mu, \sqrt{1-\mu^2} \cos \Phi, \sqrt{1-\mu^2} \sin \Phi). \quad (20)$$

The four-momentum vector of a neutrino is given by

$$p^\nu = \epsilon u^\nu, \quad (21)$$

where ϵ is the energy of the neutrino.

These three dimensions in momentum space and three dimensions in real space constitute the six-dimensional phase space. The distribution of neutrinos in this phase space is given by $f(r, \theta, \phi, \epsilon, \mu, \Phi)$. The four-current of particles in the phase space cell $d\Gamma_{\text{com}}$ is given by

$$j^\mu = \int f u^\mu d\Gamma_{\text{com}}. \quad (22)$$

The number ΔN of particles in $d\Gamma_{\text{com}}$ within some 3-volume is

$$\begin{aligned} \Delta N &= \int \sqrt{-g} \langle \mathbf{j}, dx^\mu \rangle \wedge dx^\nu \wedge dx^\xi \wedge dx^\sigma \\ &= \int \sqrt{-g} j^\mu dx^\nu dx^\xi dx^\sigma, \end{aligned} \quad (23)$$

where $\langle \mathbf{j}, dx^\mu \rangle$ denotes the contraction of the 4-vector \mathbf{j} with the volume form. This general form can be used to obtain both the number of particles within a space-like three-volume cell d^3x as well as the number of particles flowing through cell interfaces per coordinate time dt (two space dimensions and one time dimension).

⁴ These hexahedra are not the same as the wedges of a spherical polar grid, as all their faces are flat.

⁵ Neutrinos become important to the dynamics of core-collapse supernovae at MeV energy scales, at which their velocities are close to the speed of light c . Thus we may employ the massless approximation of neutrinos, i.e. approximating their velocity as c such that their velocities satisfy $\|u^\nu\| = 0$.

The number of particles within the phase space volume $d\Gamma_{\text{com}}$ in a cell $dx^1 dx^2 dx^3$ is

$$N = \iiint \sqrt{-g} f u^0 d\Gamma_{\text{com}} dx^1 dx^2 dx^3, \quad (24)$$

and the flux across a cell interface with $x_1 = \text{const.}$ is

$$F = \iiint \sqrt{-g} f u^1 d\Gamma_{\text{com}} dx^2 dx^3 dt. \quad (25)$$

For a conformally flat metric (Isenberg 2008) (used in CoCoNuT), with

$$g_{\mu\nu} = \begin{pmatrix} -\alpha^2 + \beta_i \beta^i & \beta_x & \beta_y & \beta_z \\ \beta_x & \phi^4 & 0 & 0 \\ \beta_y & 0 & \phi^4 & 0 \\ \beta_z & 0 & 0 & \phi^4 \end{pmatrix}, \quad (26)$$

in terms of the lapse function α , the conformal factor ϕ , the shift vector β^i , and $\beta_i = \phi^4 \beta^i$, these can be simplified to

$$N = \iiint \phi^6 f \hat{u}^0 d\Gamma_{\text{com}} dx^1 dx^2 dx^3, \quad (27)$$

$$F = \iiint \phi^6 f \left(\frac{\alpha}{\phi^2} \hat{u}^1 + \beta^r \hat{u}^0 \right) d\Gamma_{\text{com}} dx^2 dx^3 dt. \quad (28)$$

in terms of the Eulerian velocity components \hat{u}^μ . It is critical to recognise that because of the invariance of the distribution function we can directly use f in the *comoving* frame to compute the number of neutrinos within phase space cell $d\Gamma_{\text{com}^\nu}$ that cross a zone boundary during the time interval dt . Only the neutrino four-velocity in Equation (22) must be transformed into the coordinate frame. The problem, however, is that the current j^μ only obeys a conservation law $\nabla_\mu j^\mu = 0$ if we define $d\Gamma_{\text{com}}$ away from a given reference point x^μ as the phase space volume filled by particles from $d\Gamma_{\text{com}}$ at x^μ (or in technical terms if we define $d\Gamma_{\text{com}}$ away from x^μ by an exponential map). In general the exponential map of $d\Gamma_{\text{com}}(x^\mu)$ from x^μ to another point x'^μ will *differ* from the momentum space volume $d\Gamma_{\text{com}}(x'^\mu)$ defined by the same comoving-frame momentum space coordinates, which necessitates the remapping step that we outlined in Section 2.1 and will specify in detail in the next section.

3.2 Mapping to destination cells

As explained in Section 2.1 the momentum coordinate of a spatially advected particle in its destination cell will not be the same as in the cell it originated from. Rather than handling these shifts using derivatives in the Boltzmann equation, we deposit the arriving neutrino into a linear combination of the nearest eight cells in momentum space (Figure 4). As a neutrino arrives in a spatial cell with momentum $p_* = (\epsilon_*, \mu_*, \Phi_*)$ after it undergoes the full chain of transformations

$$\tilde{u}_{\text{dst}} = \Lambda_{\text{dst}}^{-1} M_{\text{dst}}^{-1} G(K(M_{\text{src}} \Lambda_{\text{src}} \tilde{u}_{\text{src}})) \quad (29)$$

(the formal expression of Equation 5), it is split between the two nearest cells in each coordinate in momentum space with weights such that both the energy, number, and direction of the neutrino are conserved, which amounts to a trilinear interpolation.

In order to write down finite-difference equations for the entire scheme, it will be useful to formally interpret the momentum-dependent distribution function as a vector \mathbf{f} with components f_{ijk} . We can then encode the remapping procedure as a linear operator T that acts on the source distribution function \mathbf{f}_{src} to yield \mathbf{f}_{dst} ,

$$\mathbf{f}_{\text{dst}} = T[\mathbf{f}_{\text{src}}], \quad (30)$$

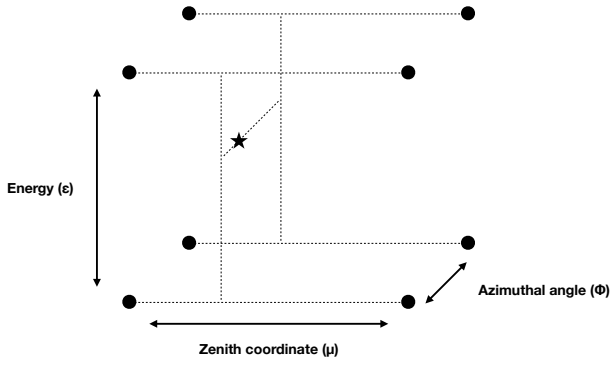


Figure 4. Illustration of the interpolation of an arriving momentum vector (star) as the linear combination of the nearest 8 vectors in the basis of the destination cell (dots). This method conserves energy and propagation angle of the net momentum vector by construction.

or in component form,

$$f_{i'j'k'}^{\text{dst}} = \sum_{ijk} T_{i'j'k',ijk}^{\text{src}} f_{ijk}^{\text{src}}, \quad (31)$$

Let us now consider a single *column* of T containing the interpolation weights for neutrinos from phase space cell (i, j, k) into the eight destination cells in momentum space that bracket the four-vector \tilde{u}_{dst} in the destination cell (Figure 4). The only non-zero matrix elements in this column are those for the cells immediately to the left (L) or right (R) of \tilde{u}_{dst} with $i' = i_{\text{L/R}}$, $j' = j_{\text{L/R}}$, and $k' = k_{\text{L/R}}$. For example, i_{L} and i_{R} are the two adjacent indices that fulfil $\epsilon_{i_{\text{L}}} \leq \epsilon_* \leq \epsilon_{i_{\text{R}}}$. To obtain the correct trilinear interpolation weights, we factor these matrix elements into interpolation weights $w_{i_{\text{L/R}}}$, $w_{j_{\text{L/R}}}$, and $w_{k_{\text{L/R}}}$ for the ϵ -, μ -, and Φ - direction,

$$T_{i_{\text{L/R}}j_{\text{L/R}}k_{\text{L/R}},ijk} = w_{i_{\text{L/R}}} w_{j_{\text{L/R}}} w_{k_{\text{L/R}}}. \quad (32)$$

Requiring neutrino number conservation leads to the condition,

$$\sum_{i'=i_{\text{L}},i_{\text{R}}} \sum_{j'=j_{\text{L}},j_{\text{R}}} \sum_{k'=k_{\text{L}},k_{\text{R}}} w_{i'} w_{j'} w_{k'} f_{ijk}^{\text{src}} = f_{ijk}^{\text{src}}. \quad (33)$$

To fulfil this condition, we choose the weights such that

$$w_{i_{\text{L}}} + w_{i_{\text{R}}} = 1, \quad (34)$$

$$w_{j_{\text{L}}} + w_{j_{\text{R}}} = 1, \quad (35)$$

$$w_{k_{\text{L}}} + w_{k_{\text{R}}} = 1. \quad (36)$$

Similarly, to conserve the direction of the neutrinos, the weights need to fulfill

$$\mu_* = \mu_{\text{L}} w_{j_{\text{L}}} + \mu_{\text{R}} w_{j_{\text{R}}}, \quad (37)$$

$$\cos(\Phi_*) = \cos(\Phi_{\text{L}} w_{k_{\text{L}}}) + \cos(\Phi_{\text{R}} w_{k_{\text{R}}}), \quad (38)$$

$$\sin(\Phi_*) = \sin(\Phi_{\text{L}} w_{k_{\text{L}}}) + \sin(\Phi_{\text{R}} w_{k_{\text{R}}}), \quad (39)$$

where $\mu_{\text{L}} \leq \mu_* \leq \mu_{\text{R}}$ and $\Phi_{\text{L}} \leq \Phi_* \leq \Phi_{\text{R}}$. To conserve energy of the neutrinos, the weights need to fulfill

$$\epsilon_* = \epsilon_{\text{L}} w_{i_{\text{L}}} + \epsilon_{\text{R}} w_{i_{\text{R}}}, \quad (40)$$

where $\epsilon_{\text{L}} \leq \epsilon_* \leq \epsilon_{\text{R}}$.

This mapping procedure forms the core of our scheme, and used to connect cells in different points in space. It requires only the transformation of a momentum vector between two frames to be

known, circumventing the need to manually implement the special and general relativistic derivative terms in the Boltzmann equation.

This procedure is also applied as particles travel forward in time. As the metric and background fluid velocity evolves, we simply remap the distribution function in each cell at the beginning of each timestep using Equation (30), calculating M_{src} and Λ_{src} using values from the previous timestep, M_{dst} and Λ_{dst} using values from the current timestep, and K using the metric from the previous and current timestep. Since particles are not travelling across the spatial grid, the geometric rotations do not apply, but relativistic boosts to their velocity can still cause them to move between angular bins.

While we implement our scheme on a spherical polar grid, this remapping procedure allows it to be adapted to any arbitrary grid geometry with minimal modifications. In a traditional implementation with derivatives, this would require major re-writing of code.

We now need to work out the precise form of the Lorentz transform Λ , the transform M from the Eulerian frame to the coordinate frame, and the transformation operators G and K for the geometric rotation and Hamiltonian “kick” between two points in space.

3.2.1 Geometric rotations

When calculating fluxes between adjacent cells in the angular direction, the coordinates frames are rotated since the momentum space coordinates are aligned with the radial direction. The three-velocity of the arriving neutrino, after all relativistic boosts have been performed, must be rotated by an angle in the direction opposite to the direction of travel. Since this only needs to be performed for adjacent cells, the frames are only ever rotated in the θ - or ϕ -direction, but not both simultaneously.

The rotation of an arbitrary three-vector \mathbf{u} about a unit vector \mathbf{k} by angle β is given by

$$\mathbf{u}' = \cos\beta \mathbf{u} + \sin\beta (\mathbf{k} \times \mathbf{u}) + (\mathbf{k} \cdot \mathbf{u}) (1 - \cos\beta) \mathbf{k}. \quad (41)$$

The zeroth component of the four-velocity is unaffected by the rotation, so the operator G acting on the four-vector (u^0, \mathbf{u}) is just

$$G(u^0, \mathbf{u}) = (u^0, \cos\beta \mathbf{u} + \sin\beta (\mathbf{k} \times \mathbf{u}) + (\mathbf{k} \cdot \mathbf{u}) (1 - \cos\beta) \mathbf{k}). \quad (42)$$

The shift necessary for a neutrino travelling in the θ -direction is a rotation by $\beta = -\Delta\theta$ around $\mathbf{k} = (0, 0, 1)$ in the momentum space coordinates. Similarly, the shift necessary for a neutrino travelling in the ϕ direction is a rotation by $\beta = -\Delta\phi$ around $\mathbf{k} = (\sin\theta, \cos\theta, 0)$.

3.2.2 Lorentz boosts

In our scheme, the neutrino source terms are always computed in the comoving frame, and similarly, the momentum grid is also defined in the comoving frame. Where the fluid velocity is non-zero, the neutrino velocity must first be transformed into the Eulerian frame to calculate fluxes across the cell interfaces, and then transformed into the comoving frame of the destination cell to determine the momentum bin that the neutrino arrives into.

The boosted neutrino velocity is

$$\hat{u}^\mu = \Lambda^\mu_\nu \tilde{u}^\nu, \quad (43)$$

where \tilde{u} is the comoving velocity, \hat{u} is the Eulerian velocity, and Λ

is the usual Lorentz boost matrix,

$$\Lambda = \begin{pmatrix} \gamma & \gamma v_r & \gamma v_\theta & \gamma v_\phi \\ \gamma v_r & 1 + (\gamma - 1) \frac{v_r^2}{v^2} & (\gamma - 1) \frac{v_r v_\theta}{v^2} & (\gamma - 1) \frac{v_r v_\phi}{v^2} \\ \gamma v_\theta & (\gamma - 1) \frac{v_\theta v_r}{v^2} & 1 + (\gamma - 1) \frac{v_\theta^2}{v^2} & (\gamma - 1) \frac{v_\theta v_\phi}{v^2} \\ \gamma v_\phi & (\gamma - 1) \frac{v_\phi v_r}{v^2} & (\gamma - 1) \frac{v_\phi v_\theta}{v^2} & 1 + (\gamma - 1) \frac{v_\phi^2}{v^2} \end{pmatrix}. \quad (44)$$

Here, \mathbf{v} is the velocity of the fluid with respect to the Eulerian frame, and $\gamma = (1 - v^2)^{-1/2}$ is the Lorentz factor. When computing fluxes across all interfaces, we will encounter γv_r , γv_θ , and γv_ϕ terms again in the Lorentz boost. Physically, these terms are the fluid advection contributions to the neutrino transport. To ensure the stability of the scheme, these components are always handled using the upwind scheme as described in Section 3.3.2.

3.2.3 Frame transformations

The matrix M^μ_ν which transforms from the orthonormal Eulerian basis to the coordinate basis,

$$u^\mu = M^\mu_\nu \hat{u}^\nu, \quad (45)$$

needs to be chosen such that $M^\mu_\alpha g_{\mu\nu} M^\nu_\beta = \eta_{\alpha\beta}$. For a general metric, this amounts to performing a Cholesky decomposition. Given a conformally flat metric, the transformation matrix and its inverse are given by

$$M = \begin{pmatrix} \alpha^{-1} & 0 & 0 & 0 \\ \alpha^{-1} \beta^x & \phi^{-2} & 0 & 0 \\ \alpha^{-1} \beta^y & 0 & \phi^{-2} & 0 \\ \alpha^{-1} \beta^z & 0 & 0 & \phi^{-2} \end{pmatrix}, \quad (46)$$

$$M^{-1} = \begin{pmatrix} \alpha & \phi^2 \beta^x & \phi^2 \beta^y & \phi^2 \beta^z \\ 0 & \phi^2 & 0 & 0 \\ 0 & 0 & \phi^2 & 0 \\ 0 & 0 & 0 & \phi^2 \end{pmatrix}. \quad (47)$$

3.2.4 Ricci rotation of velocity components between cells

In order to properly handle geodesic transport of particles between cells, we consider the equation of motion for the covariant velocity components,

$$u_\mu = g_{\mu\nu} u^\nu, \quad (48)$$

which can be obtained from the super-Hamiltonian $H = g^{\mu\nu} u_\mu u_\nu$ with the covariant components u_μ serving as the canonical ‘‘momenta’’ (Misner et al. 1973), as

$$\frac{du_\mu}{d\lambda} = - \frac{\partial g^{\alpha\beta}}{\partial x^\mu} u_\alpha u_\beta. \quad (49)$$

Since the Hamiltonian does not depend on the affine parameter (or canonical ‘‘time’’) λ , its value is conserved along geodesics,

$$\frac{d}{d\lambda} (g^{\alpha\beta} u_\alpha u_\beta) = 0. \quad (50)$$

If the metric is taken to vary discretely from one cell to the next, particles receive a Hamiltonian ‘‘kick’’ $u_{\text{src}} \rightarrow u_{\text{dst}}$ when crossing a cell interface. The kick can be calculated from the discrete version of Equation (50):

$$g_{\text{dst}}^{\mu\nu} u_{\mu,\text{dst}} u_{\nu,\text{dst}} = g_{\text{src}}^{\mu\nu} u_{\mu,\text{src}} u_{\nu,\text{src}}. \quad (51)$$

Note that since the Hamiltonian varies only along one coordinate direction across a cell interface, only the covariant velocity component u_i in the direction of the i -th coordinate will receive a kick according to Equation (49).

Now define $\delta g^{\mu\nu} = g_{\text{dst}}^{\mu\nu} - g_{\text{src}}^{\mu\nu}$ and

$$\delta u_\mu = \begin{cases} \delta, & \mu = i \\ 0, & \mu \neq i \end{cases}, \quad (52)$$

which allows us to rewrite Equation (51) as

$$g_{\text{dst}}^{\mu\nu} \delta u_\mu \delta u_\nu + 2g_{\text{dst}}^{\mu\nu} u_{\mu,\text{src}} \delta u_\nu + \delta g^{\mu\nu} u_{\mu,\text{src}} u_{\nu,\text{src}} = 0, \quad (53)$$

and in terms of δ as

$$g_{\text{dst}}^{ii} \delta^2 + 2g_{\text{dst}}^{ii} u_{i,\text{src}} \delta + \delta g^{\mu\nu} u_{\mu,\text{src}} u_{\nu,\text{src}} = 0. \quad (54)$$

This is a quadratic equation for δ , which formally has two solutions,

$$\delta = \frac{-g_{\text{dst}}^{ii} u_{i,\text{src}} \pm \sqrt{(g_{\text{dst}}^{ii} u_{i,\text{src}})^2 - g_{\text{dst}}^{ii} \delta g^{\mu\nu} u_{\mu,\text{src}} u_{\nu,\text{src}}}}{g_{\text{dst}}^{ii}}. \quad (55)$$

The plus solution is the correct solution for $u_{i,\text{src}} > 0$, as it satisfies $\delta \rightarrow 0$ for $\delta g^{\mu\nu} \rightarrow 0$. Similarly, the minus solution is the correct solution for $u_{i,\text{src}} < 0$. A complication to this method arises if the kick necessary to conserve the Hamiltonian results in a velocity in the opposite direction through the interface, akin to the phenomenon of total internal reflection in refractive media. This manifests mathematically as the quadratic equation yielding no real solutions. We circumvent the issue by modifying the kick to become

$$\delta = -u_{i,\text{src}}, \quad (56)$$

and then scaling the other spatial components of u so that energy is conserved. While this results in a small loss of momentum conservation, the error is insignificant in comparison to the error arising from the grid discretisation, and such cases only arise in the presence of extremely steep gradients in the metric. In summary, the kicked four-velocity is

$$u_{\text{dst}} = K(u_{\text{src}}), \quad (57)$$

where

$$K(u_{\text{src}})^\mu = g_{\text{dst}}^{\mu\nu} (u_{\nu,\text{src}} + \delta u_{\nu,\text{src}}). \quad (58)$$

3.3 Computation of fluxes and update of the distribution function

We express Equation (1) as the three-dimensional (unsplit) difference equation,

$$\frac{f^{n+1} - f^n}{\Delta t} + \sum_{s \in \{a \pm \frac{1}{2}, b \pm \frac{1}{2}, c \pm \frac{1}{2}\}} \left[\mathbf{u} \cdot \mathbf{n}_s (T_{s \rightarrow a,b,c} [\mathbf{f}_s^n])_{ijk} \frac{\Delta A_s}{\Delta V_{abc}} \right] = \mathfrak{C} [\mathbf{f}_{abc}]. \quad (59)$$

Here Δt is the timestep and ΔV is the cell volume. The advection term is summed over every interface s of the cell, where ΔA_s is the interface area, \mathbf{n}_s is the interface normal. The neutrino advection velocity \mathbf{u} is given by the contravariant spatial components of the *four-velocity* at cell interfaces. The transformation operator T is computed as explained in the previous sections; the subscript $s \rightarrow abc$ indicates that the transformation remaps the distribution function \mathbf{f}_s^n at the interface s from interface frame to the comoving frame in cell (a, b, c) in real space. For compactness and readability, we have omitted real space and momentum space indices for f , \mathbf{u} , and the discretised collision integral \mathfrak{C} (for which see Equation 66 below).

Equation (59) gives an updated distribution function in cell (a, b, c) , but this updated distribution function is still computed in the comoving frame from the previous time step. After accounting

for updates to the distribution function due to the fluxes at cell interfaces and due to the collision integral, we therefore still need to boost the distribution function at time step $n + 1$ from the comoving frame at time step n to the comoving frame at time step $n + 1$,

$$\mathbf{f}^{n+1} \rightarrow T_{n \rightarrow n+1}[\mathbf{f}^{n+1}]. \quad (60)$$

This completes the transport time step.

In Sections 3.3.1–3.3.3, we will show how f_s is obtained via either a Lax-Wendroff step, or an upwind step with linear reconstruction, both of which result in second-order convergence in space. For time integration, although the convergence of the advection terms is also second-order, the convergence of the collision term is only first-order due to the backward Euler differencing, which is usual for most transport codes. Defining the accuracy in angle and energy is non-trivial, given our particle-like treatment.

In optically thick regions, the source term is stiff, which would necessitate a restrictively small timestep in order to maintain stability in a fully explicit scheme. We circumvent this restriction by discretising the source term implicitly in time (coupling the momentum space in a matrix inversion), while still solving the advection terms explicitly to avoid coupling in real space. For simplicity, we use a global timestep, limited by the Courant number in the smallest cell on the grid.

3.3.1 Lax-Wendroff scheme

To recover the correct solution in the diffusion limit, we employ the Lax-Wendroff scheme, which provides second-order accuracy in both time and space. This amounts to replacing each $\mathbf{f}_s^{n+\frac{1}{2}}$, which is solved by advancing the solution by half a timestep in each spatial direction. For example, in the a direction, this amounts to solving

$$\frac{f_{a+\frac{1}{2}}^{n+\frac{1}{2}} - \frac{1}{2} \left(T_{a \rightarrow a+\frac{1}{2}}[\mathbf{f}_a^n] + T_{a+1 \rightarrow a+\frac{1}{2}}[\mathbf{f}_{a+1}^n] \right)_{ijk}}{\frac{1}{2} \Delta t} + \left(\mathbf{u} \cdot \mathbf{n}_{a+\frac{1}{2}} \right) \frac{\left(T_{a+1 \rightarrow a+\frac{1}{2}}[\mathbf{f}_{a+1}^n] - T_{a \rightarrow a+\frac{1}{2}}[\mathbf{f}_a^n] \right)_{ijk}}{\Delta x} = \mathbb{C}[\mathbf{f}_{a+\frac{1}{2}}^{n+\frac{1}{2}}]. \quad (61)$$

Here, $\Delta x = x_{a+1} - x_a$ is the distance between the cell centers. This equation is solved in the interface frame, so all transformations are to the interface frame. In the general multi-dimensional solution, this is repeated along each direction. We highlight that the $\frac{1}{2} \left(T_{a \rightarrow a+\frac{1}{2}}[\mathbf{f}_a^n] + T_{a+1 \rightarrow a+\frac{1}{2}}[\mathbf{f}_{a+1}^n] \right)$ reconstruction term (which can alternatively be implemented as a geometric mean), together with the implicitly discretised source term on the right-hand side, provides the centered differencing crucial for reproducing the diffusion limit. Again, we have omitted extra real space and momentum space indices for f , \mathbf{u} , and the collision integral \mathbb{C} , implied to be abc and ijk except where specified.

3.3.2 Upwind scheme

The spatially centered reconstruction of the Lax-Wendroff scheme produces an oscillatory solution in regions where the physical domain of dependence is one-sided, namely where the opacity is low and neutrinos stream freely. To maintain stability in these regions, we use an upwind scheme

$$f_{a+\frac{1}{2}}^n = \begin{cases} \tilde{f}_{a,ijk}^n, & \mathbf{u}_{a+\frac{1}{2},ijk} \cdot \mathbf{n}_{a+\frac{1}{2}} \geq 0 \\ \tilde{f}_{a+1,ijk}^n, & \mathbf{u}_{a+\frac{1}{2},ijk} \cdot \mathbf{n}_{a+\frac{1}{2}} < 0 \end{cases}, \quad (62)$$

where \tilde{f}_a^n and \tilde{f}_{a+1}^n are linearly reconstructed values at $x_{a+\frac{1}{2}}$. Here, \mathbf{u} is the velocity of the neutrino at the cell center expressed in the basis at the interface (i.e. $\mu = 1$ is parallel with angular interfaces), to account for the angle of the cell interface relative to the cell center. Reconstruction is performed along characteristics, taking into account boosts along the path of the neutrino between cells, which recovers second-order accuracy in space. We apply the MC slope limiter (van Leer 1977) to suppress any remaining oscillations in the solution.

3.3.3 Smooth flux switching

To achieve a smooth transition between optically thick and thin regions, we interpolate between the interface distributions calculated by the Lax-Wendroff scheme and the upwind scheme using the formulation

$$f_{a+\frac{1}{2}}^n = f_{a+\frac{1}{2},\text{LW}}^{n+\frac{1}{2}} (1 - w) + f_{a+\frac{1}{2},\text{upw}}^n w, \quad (63)$$

where the weights are motivated by the optical depth of the cell

$$w = e^{-(\kappa_a + \kappa_s) \Delta x}. \quad (64)$$

Since the neutrino opacity varies with energy, the flux switching must be performed separately for each energy cell.

3.3.4 Boundary conditions

In three dimensions, there exists on our grid formal boundaries at $r = 0$, $r = r_{\text{max}}$, $\theta = \theta_{\text{min}}$, and $\theta = \theta_{\text{max}}$. In practice, the only real boundary is at $r = r_{\text{max}}$, where we apply an outflow boundary condition. The outflow boundary condition is appropriate for CCSN modelling where there are no external sources of neutrinos, because and neutrinos are travelling radially outward near the outer boundary. In two dimensions, we apply periodic boundary conditions in the ϕ direction, such that the domain is a wedge with angular size $\Delta\phi$, which we have the freedom to choose. In one dimension, we also apply periodic conditions to the θ such that the domain is a column, again with the freedom to choose the angular size $\Delta\theta$. In practice, we have found that choosing $\Delta\phi$ and $\Delta\theta$ so that all six interfaces of cells have a similar area produces the most accurate results without unnecessary restriction by the CFL criteria.

3.4 Coupling to matter (source terms)

We model the production, absorption, and scattering of neutrinos by expressing the source term on the right-hand side of the Boltzmann equation (1) as

$$\mathbb{C}[f] = \kappa_a (f_{\text{eq}} - f) + \frac{\kappa_s}{4\pi} \int_{4\pi} f \, d\Omega - \kappa_s f, \quad (65)$$

where f_{eq} is the equilibrium value of f , κ_a is the coefficient of absorption, and κ_s is the coefficient of scattering which we assume to be elastic and isotropic for the time being. The discretised form of this equation is

$$\mathbb{C}[f_{ijk}] = \kappa_{a,i} (f_{\text{eq},i} - f_{ijk}) + \frac{\kappa_{s,i}}{4\pi} \sum_{\substack{j'=1,\dots,N_\mu \\ k'=1,\dots,N_\phi}} (f_{ijk} \Delta\Omega_{jk}) - \kappa_{s,i} f_{ijk}. \quad (66)$$

Here, we have dropped the indices a, b, c for compactness.

Since electron and antielectron neutrinos behave differently to the heavy-lepton species, and present the greatest effect on the energetics of supernovae, we adopt the commonly used three-flavour

approach, solving the transport equation independently for electron neutrinos, electron antineutrinos, and a third combined group of the remaining muon and tauon neutrinos and antineutrinos. The three-flavour approach provides a good balance between accuracy and computational efficiency, but our method can accommodate an arbitrary number of species. Eventually, with the implementation of weak magnetism terms, degeneracies between neutrinos and antineutrinos will be lifted, and more than three species will be required.

We use a subset of the neutrino interactions described by [Rampp & Janka \(2002\)](#). Using f_{eq} , κ_a , and κ_s , we model absorption onto nucleons and nuclei, the Bremsstrahlung process in the one-particle approximation ([Müller & Janka 2015](#); [O'Connor 2015](#)), and scattering on nucleons and heavy nuclei, for which the interaction rates are functions of the thermodynamic quantities of the fluid. We do not calculate non-isoenergetic scattering, which reduces the computational cost of implicitly solving the collision terms. While the set of interactions we use is incomplete, they are sufficient for the purposes of demonstrating the viability of our new scheme.

To model the backreaction of neutrinos on the fluid, we calculate hydrodynamical source terms for the lepton number, energy, and momentum

$$Q_{Y_e} = -\frac{1}{h^3} \int_{4\pi} \int_0^\infty (\mathfrak{C}_{\nu_e} - \mathfrak{C}_{\bar{\nu}_e}) d\epsilon d\Omega, \quad (67)$$

$$Q_E = -\frac{1}{h^3} \int_{4\pi} \int_0^\infty \left(\sum_{\nu_e, \bar{\nu}_e, \nu_\mu, \bar{\nu}_\mu} \mathfrak{C} \right) \epsilon d\epsilon d\Omega, \quad (68)$$

$$Q_M = -\frac{1}{h^3} \int_{4\pi} \int_0^\infty \left(\sum_{\nu_e, \bar{\nu}_e, \nu_\mu, \bar{\nu}_\mu} \mathfrak{C} \right) \mathbf{p} d\epsilon d\Omega. \quad (69)$$

The distribution function should always be non-negative ($f \geq 0$), and to obey Fermi statistics, should always be bounded ($f \leq 1$). The blocking factors in the opacity coefficients should in principle guarantee both these properties, but advection of neutrinos in momentum space can still cause cells to become overpopulated. This is unavoidable in a conservative finite-volume discretisation. In practice, we find that the interpolation between Lax-Wendroff and upwind fluxes (Section 3.3.3) suppresses any non-monotonocities that might cause the distribution to become negative. However, the distribution can still overshoot beyond unity at sharp jumps in opacity (resulting in large fluxes across angular bins) or fluid velocity (resulting in large fluxes across energy bins). Naturally, this error diminishes with increasing resolution in momentum space, though this is not a computationally feasible solution. A naive correction for this error would result in a violation of conservation properties and lead to a secular drift in total number and/or energy.⁶ We instead choose to maintain conservation properties and allow the distribution function to exceed unity. The only consequence is an error in the hydrodynamical source terms (Equations 67–69). The opacity coefficients continue to be well-behaved and drive the distribution back towards $f \leq 1$, which causes the excess neutrinos to be absorbed back into the matter, where they may then be re-emitted into a higher energy bin. All in all, the transient overpopulation of lower energy bins results in a larger fraction of neutrinos interacting less strongly with the matter, which increases the trapping density.

⁶ Fixes have been devised to restore conservation at the expense of internal energy drift ([Mezzacappa & Bruenn 1993b](#); [Liebendörfer et al. 2004](#))

3.5 Implicit solution of the source terms

In general, the solutions to Equations (59) and (61) can be found by solving a $N_\epsilon \times N_\mu \times N_\Phi$ linear system which couple together the ϵ , μ , and Φ dimensions. By approximating all scattering as elastic, this can be reduced to N_ϵ independent $N_\mu \times N_\Phi$ systems. We assume that scattering is both elastic and isotropic (65), for which there exists the computationally economical analytic solution

$$f_{jk}^{n+1} = \frac{1}{1 + (\kappa_a + \kappa_s)\Delta t} \times \left[f_{jk}^n + \Delta t \kappa_a f_{\text{eq}} \right. \\ \left. + \frac{\kappa_s \Delta t}{4\pi} \frac{\sum_{j'k'} (f_{j'k'}^n + \Delta t \kappa_a f_{\text{eq}} + \Delta J_{j'k'}) \Delta \Omega}{1 + (\kappa_a + \kappa_s)\Delta t} + \Delta J_{jk} \right], \quad (70)$$

where ΔJ_{jk} is the advective flux divergence component of the difference equations (59, 61), and the energy index i has been omitted for all terms.

4 CODE TESTS

To demonstrate the quality of the transport scheme, we perform a suite of tests problems as described in [Rampp & Janka \(2002\)](#) and [Müller et al. \(2010\)](#), for which exact solutions can be obtained. We then demonstrate its capacity to be used in modelling a spherically symmetric core collapse supernova. Finally, we demonstrate that the scheme can handle two-dimensional transport problems with ease by performing a test in axisymmetry.

4.1 Classical radiating spheres

The radiating sphere test consists of a stationary homogeneous sphere $r \leq R$ of isotropically absorbing and emitting medium $f_{\text{eq}} = \text{const.}$ and $\kappa_a = \text{const.}$ within a vacuum $\kappa_a = 0$ for $r > R$. It is a commonly used benchmark which challenges the ability of radiative transfer methods to accurately model the transition from the diffusive to the free-streaming regime. The discontinuous jump in opacity poses a challenge even for state-of-the-art analytic two-moment closure methods, which have difficulty correctly reproducing the correct flux factor ([Murchikova et al. 2017](#)). It is a simple emulation of a supernova, where neutrinos escape the dense diffusive matter of the proto-neutron star though the discontinuity provides a more challenging transition compared to a real proto-neutron star surface. Nonetheless, the late-phase emission more closely resembles the homogeneous sphere test because the density gradient at the proto-neutron star surface becomes steeper. Demonstrating that a scheme is capable of reproducing the radiating sphere solution is the first step to proving its capacity to model CCSNe from core bounce through to the neutrino-driven wind phase. The analytic solution to this problem (e.g. [Smit et al. 1997](#)), as a function of radius r and radiation angle μ is

$$f(r, \mu) = f_{\text{eq}} \left(1 - e^{-\kappa_a s(r, \mu)} \right) \quad (71)$$

where

$$s(r, \mu) = \begin{cases} r\mu + rg(r, \mu), & r < R, -1 \leq \mu \leq 1 \\ 2Rg(r, \mu), & r \geq R, \sqrt{1 - \left(\frac{r}{R}\right)^2} \leq \mu \leq 1 \\ 0, & \text{else} \end{cases}, \quad (72)$$

and

$$g(r, \mu) = \sqrt{1 - \left(\frac{r}{R}\right)^2} (1 - \mu^2). \quad (73)$$

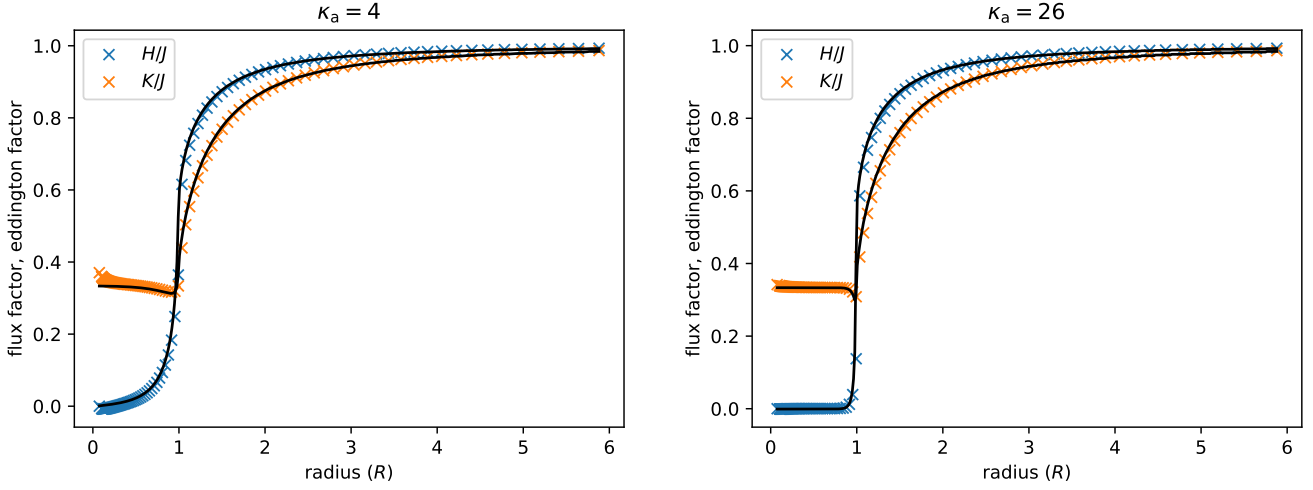


Figure 5. Radiating sphere test for $\tau = 4$ representing “low” opacity (left) and $\tau = 26$ representing “high” opacity. The flux factor and Eddington factor of the numerical solution (crosses) are compared against the exact solution (lines).

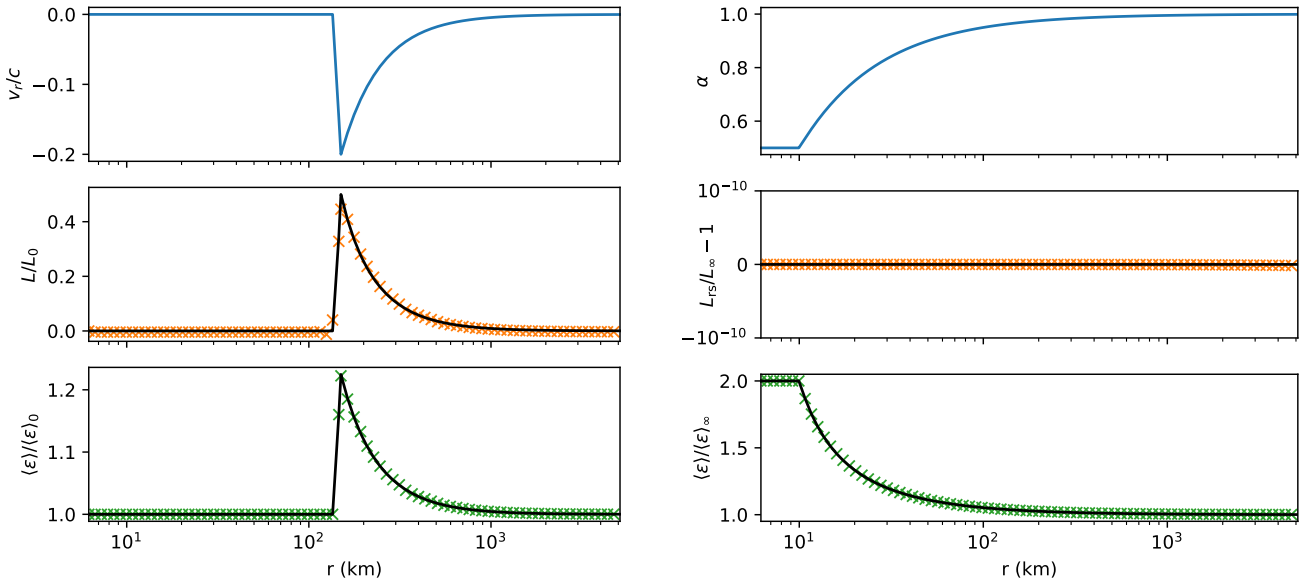


Figure 6. Setup and results of relativistic radiating sphere tests, repeating Müller et al. (2010). Left: Radiating sphere with a shock velocity profile (top). We show the luminosity L (middle) and mean energy $\langle \epsilon \rangle$ (bottom) as measured by a moving observer, normalised to the values L_0 and $\langle \epsilon \rangle_0$ just outside the radiating sphere, of our scheme (crosses) compared with the exact solution (lines). There is no redshift correction because there is no gravitational field. Right: Radiating sphere in a gravitational well (top). We show the redshift-corrected luminosity L_{rs} (middle) and mean energy $\langle \epsilon \rangle$ (bottom) as measured by a moving observer, normalised their the values at infinity L_∞ and $\langle \epsilon \rangle_\infty$, of our scheme (crosses) compared to the exact solution (lines).

We repeat the radiating sphere tests performed by Rampp & Janka (2002) and compare to the analytic solutions. We adopt a spatial resolution of $N_r = 100$ logarithmically spaced zones, an angular resolution of $N_\mu = 9$ and $N_\phi = 4$, and a domain of $r_{\max} = 6R$. For the initial conditions $f = 0$ everywhere. After a stationary state is reached, the flux factor H/J and Eddington factor K/J are compared with the exact solution. Here, J, H, K are the zeroth, first, and second energy moments given by

$$J = \frac{1}{4\pi} \int_{4\pi} f \epsilon \frac{d\Omega \epsilon^2 d\epsilon}{h^3}, \quad (74)$$

$$H = \frac{1}{4\pi} \int_{4\pi} f \mu \epsilon \frac{d\Omega \epsilon^2 d\epsilon}{h^3}, \quad (75)$$

$$K = \frac{1}{4\pi} \int_{4\pi} f \mu^2 \epsilon \frac{d\Omega \epsilon^2 d\epsilon}{h^3}. \quad (76)$$

It is useful to perform this test at varying optical depths $\tau = \kappa_a R$. We adopt the same two test parameters as Rampp & Janka (2002), one with low optical depth $\tau = 4$ and one with high optical

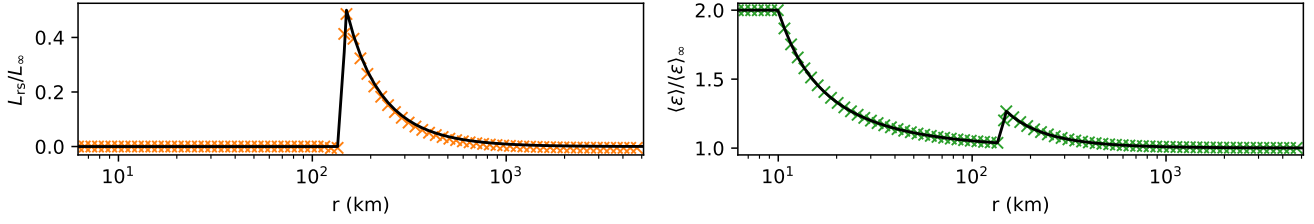


Figure 7. Radiating sphere, combining the shock velocity profile and gravitational well of the previous two tests. We show the redshift-corrected luminosity L_{rs} (left) and mean energy $\langle \epsilon \rangle$ (right) as measured by a moving observer, normalised their the values at infinity L_∞ and $\langle \epsilon \rangle_\infty$, of our scheme (crosses) compared to the exact solution (lines).

Table 1. Mean square deviation (Equation (27) of Murchikova et al. 2017) of the flux factor and Eddington factor between $R < r < 2R$ for the radiating sphere test with $\tau = 7500$. The first row (Boltzmann) shows the error of our scheme. The remaining rows show the error of commonly used closure relations from the results of Murchikova et al. (2017).

Method	$\delta(H/J)$	$\delta(K/J)$
Boltzmann	0.03	0.03
Kershaw	0.13	0.32
Wilson	0.05	0.14
Levermore	0.10	0.22
ME	0.07	0.17
MEFD	0.07	0.17
Janka_1	0.07	0.13
Janka_2	0.10	0.21

depth $\tau = 26$. In both cases, we find excellent agreement with the analytic solution (5). Near the center, there is a slight deviation, an artefact of the grid singularity. The error is less pronounced at higher opacities. We also repeat the test by Murchikova et al. (2017) using $\tau = 7500$. We compare the error of our scheme against the error of the closure schemes used in their test, and find that our scheme outperforms them all (Table 1).

4.2 Relativistic radiating spheres

We then proceed by repeating three tests from Müller et al. (2010). We specify the test parameters in CGS units for ease of comparison to a real core-collapse and the existing literature (Müller et al. 2010; O’Connor 2015). The first test verifies the scheme’s ability to accurately account for Lorentz boosts. In this test (Figure 6, left), an optically thick radiating sphere is surrounded by a velocity profile similar to that of a stalled shock. The radiating sphere has a radius of 4 km, embedded in a velocity field

$$v_r = \begin{cases} 0, & r < 135 \text{ km} \\ -0.2c \frac{r-135 \text{ km}}{15 \text{ km}}, & 135 \text{ km} \leq r \leq 150 \text{ km} \\ -0.2c \left(\frac{150 \text{ km}}{r} \right)^2, & 150 \text{ km} \leq r \end{cases} \quad (77)$$

The second test (Figure 6, right) verifies the scheme’s ability to accurately account for gravitational redshift in the presence of a curved spacetime. In this test, the same optically thick radiating sphere is embedded into a gravitational potential

$$\alpha = \begin{cases} 0.5, & r < 10 \text{ km} \\ 0.5 + 0.5 \times \left(1 - \frac{10 \text{ km}}{r} \right), & r \geq 10 \text{ km} \end{cases} \quad (78)$$

The central value of the lapse function is $\alpha = 0.5$ and gradient $\frac{d\alpha}{dr}$

is more extreme than in a typical core-collapse supernova, and thus provides a good demonstration of the robustness of our scheme. In particular, we deliberately include a discontinuity in $\frac{d\alpha}{dr}$ at 10 km to probe for any stability issues. We set the conformal factor to $\phi = \alpha^{-1/2}$.

The third test (Figure 7) is a combination of the first two. To demonstrate our scheme’s ability to handle even the most difficult scenarios, we choose $\kappa_a = 100$ to obtain an optically thick sphere in *only* the highest energy cell, and $\kappa_a = 0$ everywhere else, resulting in a discontinuity in energy space. We use $N_\epsilon = 12$ energy cells ranging from 4 MeV to 240 MeV for a modest energy resolution of $\Delta\epsilon/\epsilon \approx 0.36$.

We test for the accurate advection of neutrinos in energy space by comparing the redshift-corrected luminosity

$$L_{rs} = 16\pi\alpha^2\phi^4 Hr^2 \quad (79)$$

and the mean energy $\langle \epsilon \rangle = H/\mathcal{H}$ as measured in the comoving observer frame with the analytic solutions. Here,

$$\mathcal{H} = \frac{1}{4\pi} \int_{4\pi} f\mu \frac{d\Omega \epsilon^2 d\epsilon}{h^3} \quad (80)$$

is the neutrino number density. In the vacuum region outside the sphere, the collision integral vanishes, and L_{rs} and $\langle \epsilon \rangle$ as measured by a moving observer obey (Müller et al. 2010)

$$\frac{1 + v_r}{1 - v_r} L_{rs} = \text{const}, \quad \gamma(1 + v_r) \alpha \langle \epsilon \rangle = \text{const}, \quad (81)$$

where v_r is the observer velocity, which we choose to be the same as the fluid velocity, and γ is the Lorentz factor. In the second test where $v_r = 0$, L_{rs} should be constant, which our scheme reproduces excellently.

4.3 Diffusion wave

To show that our scheme is able to reproduce the correct fluxes in the diffusion limit, we test the diffusion of a Gaussian distribution in an optically thick medium. First, we test our scheme in planar geometry, which allows us to examine the Lax-Wendroff fluxes in isolation, without the rotation terms associated with the spherical polar grid. The exact solution for the evolution of a Dirac delta function in the diffusion limit is

$$E = \sqrt{\frac{\kappa_s}{t}} \exp\left(\frac{-3\kappa_s z^2}{4t}\right), \quad (82)$$

$$F = \frac{z}{2t} E. \quad (83)$$

Here, $E = 4\pi J$ is the energy density, and $F = 4\pi H$ is the energy flux. Our grid spacing is $\Delta z = 0.01$, and we set $\kappa_s = 100$ so that

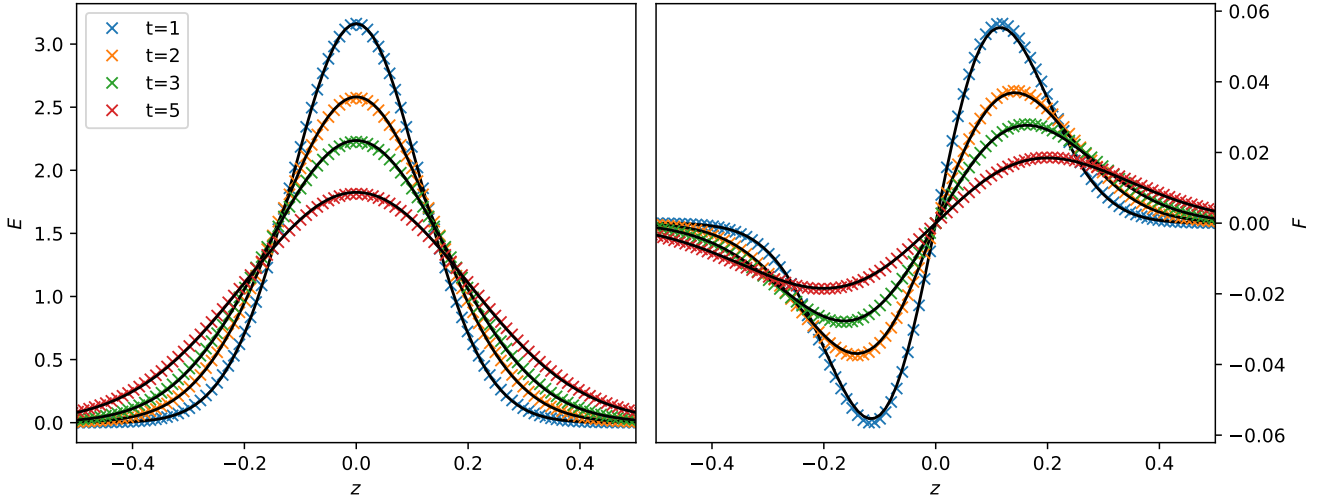


Figure 8. Diffusion wave test in planar geometry. The initial conditions are given at $t = 1$. The numerical solution is sampled at $t = 2, 3, 5$ (crosses), and compared with the exact solution (lines).

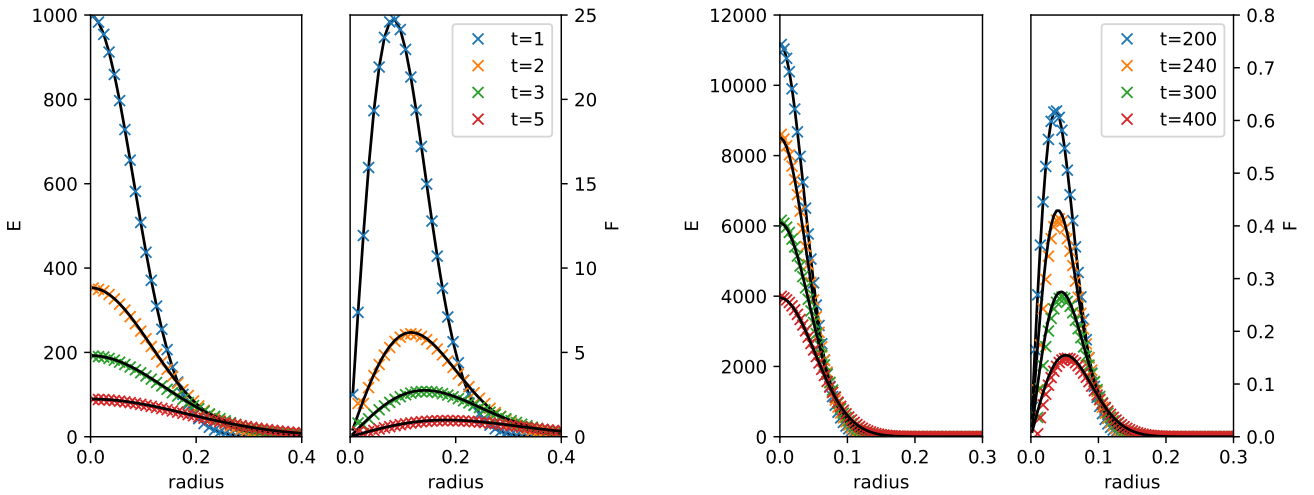


Figure 9. Diffusion wave test in spherical polar geometry, comparing the numerical solutions (crosses) to the exact solutions (lines). Left: Energy density and flux for $\kappa_s = 10^2$ ($Pe = 1$), initialised at $t = 1$ and sampled at $t = 2, 3, 5$. Right: Energy density and flux for $\kappa_s = 10^5$ ($Pe = 1000$), initialised at $t = 200$ and sampled at $t = 240, 300, 400$.

$Pe = 1$. The initial conditions are set as the exact solution at $t = 1$. We sample our numerical solution at $t = 2, 3, 5$, and find excellent agreement with the exact solution (Figure 8). Next, we perform the diffusion wave test on a spherical grid to incorporate the effect of geometric rotations. We use an identical setup to Pons et al. (2000), with $\Delta r = 0.01$, repeated for two opacities $\kappa_s = 10^2$ ($Pe = 1$) and $\kappa_s = 10^5$ ($Pe = 1000$). The exact solution in the diffusion limit is

$$E = \left(\frac{\kappa_s}{t}\right)^{3/2} \exp\left(\frac{-3\kappa_s r^2}{4t}\right), \quad (84)$$

$$F = \frac{r}{2t} E. \quad (85)$$

We again set the initial conditions as the exact solution at $t = 1$ for the $\kappa_s = 10^2$ case and $t = 200$ for the $\kappa_s = 10^5$ case. We find acceptable agreement with the exact solution in both cases (Figure

9). The small error near the grid singularity $r = 0$ is due to the interpolation between angle groups for lateral fluxes.

4.4 Core collapse in spherical symmetry

Having demonstrated that our scheme can handle these rigorous test problems, we move on to a spherically symmetric core-collapse simulation in general relativity as a test for time-dependent effects when coupled to a hydrodynamics code. We couple our Boltzmann scheme to the general relativistic hydrodynamics code CoCoNuT, and evolve a $20M_\odot$ model from collapse up to over 200 ms after bounce. The purpose of this simulation is to demonstrate that the coupling is stable and reproduces the familiar dynamics of the collapse and accretion phase. The test is not meant to rigorously quantify the accuracy of the code in dealing with the full supernova

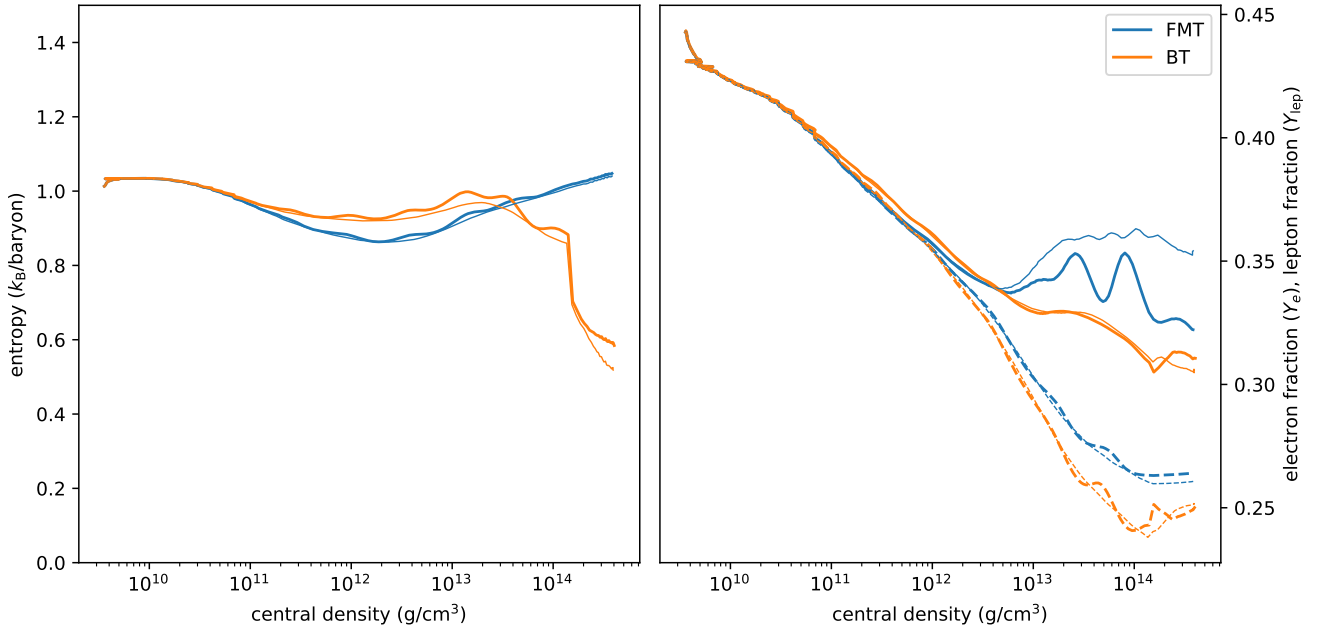


Figure 10. Central entropy (left), total lepton fraction Y_{lep} (right, solid lines), and electron fraction Y_e (right, dashed lines) as a function of central density during collapse. Blue lines show the FMT results, and orange lines show the results from our new scheme. The runs with $N_\epsilon = 12$ (thick lines) are compared with the runs with $N_\epsilon = 24$ (thin lines) to show that the cause of the oscillations at $\rho_c > 10^{12}$ g/cm³ are caused by discretisation in energy space.

problem, which would be premature for the first implementation of a completely new numerical method while upgrades are still ongoing. For the purpose at hand, it is therefore appropriate to use simplified opacities and use a relatively simple, but reasonably accurate scheme for a reference solution. Here we compare our results to the FMT scheme, which has been described and tested against the variable Eddington factor code VERTEX (Rampp & Janka 2002; Müller et al. 2010) by (Müller & Janka 2015). A more thorough validation against other 1D transport codes by a more detailed code comparison as in Liebendörfer et al. (2005); Müller et al. (2010); O’Connor (2015); Just et al. (2015); O’Connor et al. (2018) is not expedient as long as critical microphysics, i.e. neutrino-electron scattering, during the collapse phase. In the present simulation, we switch off neutrino scattering off heavy nuclei to mimic the final low- Y_e conditions in the core, but nonetheless the collapse dynamics is too different from models with more sophisticated microphysics to allow a meaningful comparison.

We adopt the same grid coordinates for the neutrino transport as the hydrodynamics. We couple the transport and the hydrodynamics solvers using an operator-split method, where the fluid quantities are first updated, and then used to compute the neutrino source terms for the next timestep. The CFL limit on the timestep for neutrino transport is smaller than that on the fluid, so we perform multiple substeps to match the hydrodynamic timestep, after which the neutrino distribution is used to compute the hydrodynamic source terms for the subsequent step. We compare the results directly with a simulation performed using the FMT scheme, keeping the initial conditions, the hydrodynamical scheme, and microphysical inputs identical, so that we can isolate the differences arising from our new transport scheme. In the following, we refer to the two runs as BT (Boltzmann transport) and FMT. In both schemes,

we use $N_\epsilon = 12$ energy cells ranging from 4 MeV to 240 MeV. In BT, we use an angular resolution of $N_\mu = 9$ and $N_\phi = 4$.

In Figure 10, we show the evolution of the entropy, electron number fraction Y_e , and total lepton number fraction $Y_{\text{lep}} = Y_e + Y_{\nu_e} - Y_{\bar{\nu}_e}$ in the core as a function of central density. During collapse, the core density ρ_c rapidly rises from $\sim 10^9$ g/cm³ to $\sim 10^{14}$ g/cm³. Neutrinos are released, corresponding to the decline in electron number. At densities below $\sim 10^{12}$ g/cm³, matter is transparent to neutrinos, allowing neutrinos escape and carry away lepton number. Since scattering off nuclei is turned off, trapping is delayed to densities considerably above $\sim 10^{12}$ g/cm³. Trapping only sets in around $\sim 10^{13}$ g/cm³ when Y_e and Y_{lep} start to diverge. We note that the electron fraction in the two runs follows a slightly different trajectory. This is because the FMT scheme does not advect trapped neutrinos but assumes instantaneous adjustment to a stationary transport solution; hence the neutrino phase-space blocking terms and the source term Q_{Y_e} for the electron fraction no longer agree in the trapping regime. After trapping the central lepton fraction should ideally remain constant if we used more accurate opacities, and after equilibrium between the matter and the neutrinos is established, the entropy should remain constant as well. However, we still find non-negligible changes in the lepton fraction and entropy beyond densities of 10^{13} g/cm³ in the BT run. This is likely due to a combination of factors. The fact that the FMT run (i.e., with a scheme that reproduces trapping if scattering off nuclei is included) shows a decrease of Y_e up to a density of 10^{14} g/cm³ suggests that without the scattering off nuclei as the major source of scattering opacity trapping simply remains incomplete until very high densities. This suggests that part of the problem lies in our choice of opacities. However, there are also indications of a numerical accuracy problem since we also note non-monotonic changes in lepton fraction and entropy above densities of 10^{14} g/cm³ where

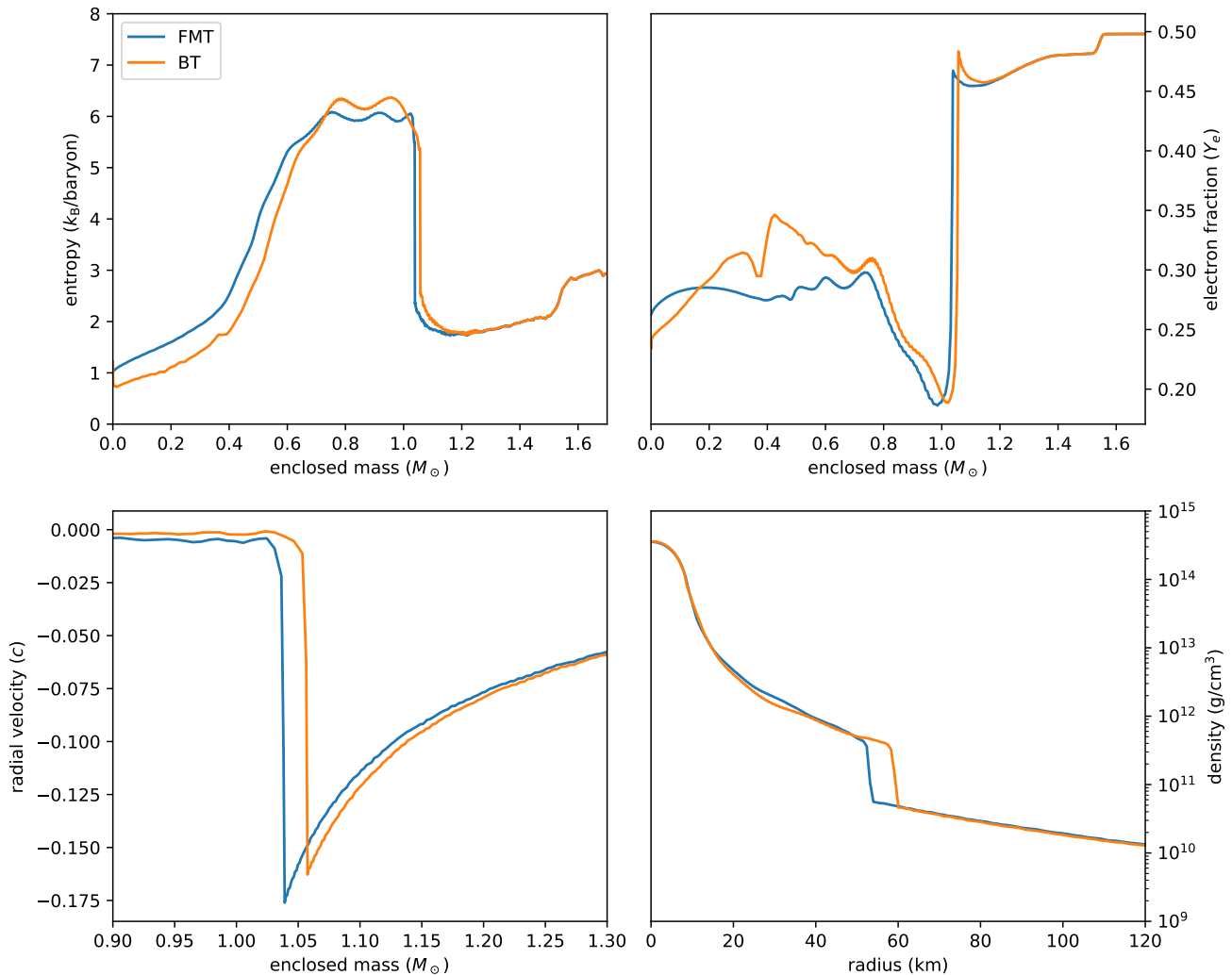


Figure 11. Profiles of the hydrodynamical quantities at 3 ms after bounce. We show entropy as a function of enclosed mass (top left), electron fraction as a function of enclosed mass (top right), radial velocity as a function of enclosed mass (bottom left), and density as a function of radius (bottom right). Blue lines show the FMT results, and orange lines show the results from our new scheme.

trapping should be complete even without coherent scattering on nuclei. The artifact seems insensitive to the energy resolution; doubling the number of energy groups did not improve entropy and lepton fraction conservation in the trapping regime.⁷ Closer inspection of the BT run reveals that a noticeable blip at the centre in the entropy and electron fraction profiles, because the neutrino flux factor does not perfectly asymptote to zero at the origin. This numerical artifact affects a few of the innermost zones, and is rather sensitive to numerical details, such as the precise choice of bound-

⁷ Note that entropy, lepton fraction, and electron fraction are also oscillatory in the FMT run from $\rho_c \sim 10^{13}-10^{14} \text{ g}/\text{cm}^3$. This is due to the low energy resolution. As discussed by Mezzacappa & Bruenn (1993a), these oscillations are caused by the finite resolution of the Fermi distribution, and become more pronounced at higher densities because the higher energy bins account for a large fraction of the phase space. Repeating the simulation using twice as many energy bins ($N_\epsilon = 24$) increases the frequency and decreases the amplitude of these oscillations, confirming that this is indeed the cause.

ary conditions. However, the blip eventually stabilises, and there is no strong long-term drift in the central entropy and electron fraction that would compromise stability during the post-bounce phase. The treatment of the innermost zones will be further optimised in future runs with more complete opacities.

After bounce, BT produces the expected behaviour in the hydrodynamics and the neutrino emission. We adopt the commonly used definition of bounce as the time when the core entropy first exceeds $3 k_B/\text{baryon}$. The mass enclosed within the radius of shock formation is $0.52 M_\odot$ in BT and $0.44 M_\odot$ in FMT. In Figure (11), we show radial profiles of the hydrodynamic quantities 3 ms after bounce. Aside from an insignificant difference in the position of the shock, the two runs agree reasonably well. BT is able to stably follow the propagation of the shock from the optically thick to the optically thin regime.

In Figure (12), we show the neutrino luminosities as measured by an observer at a radius of 500 km. The peak in BT is delayed by 2 ms because the burst takes a small amount of time to reach 500 km, whereas the luminosity at the observer radius instantly in-

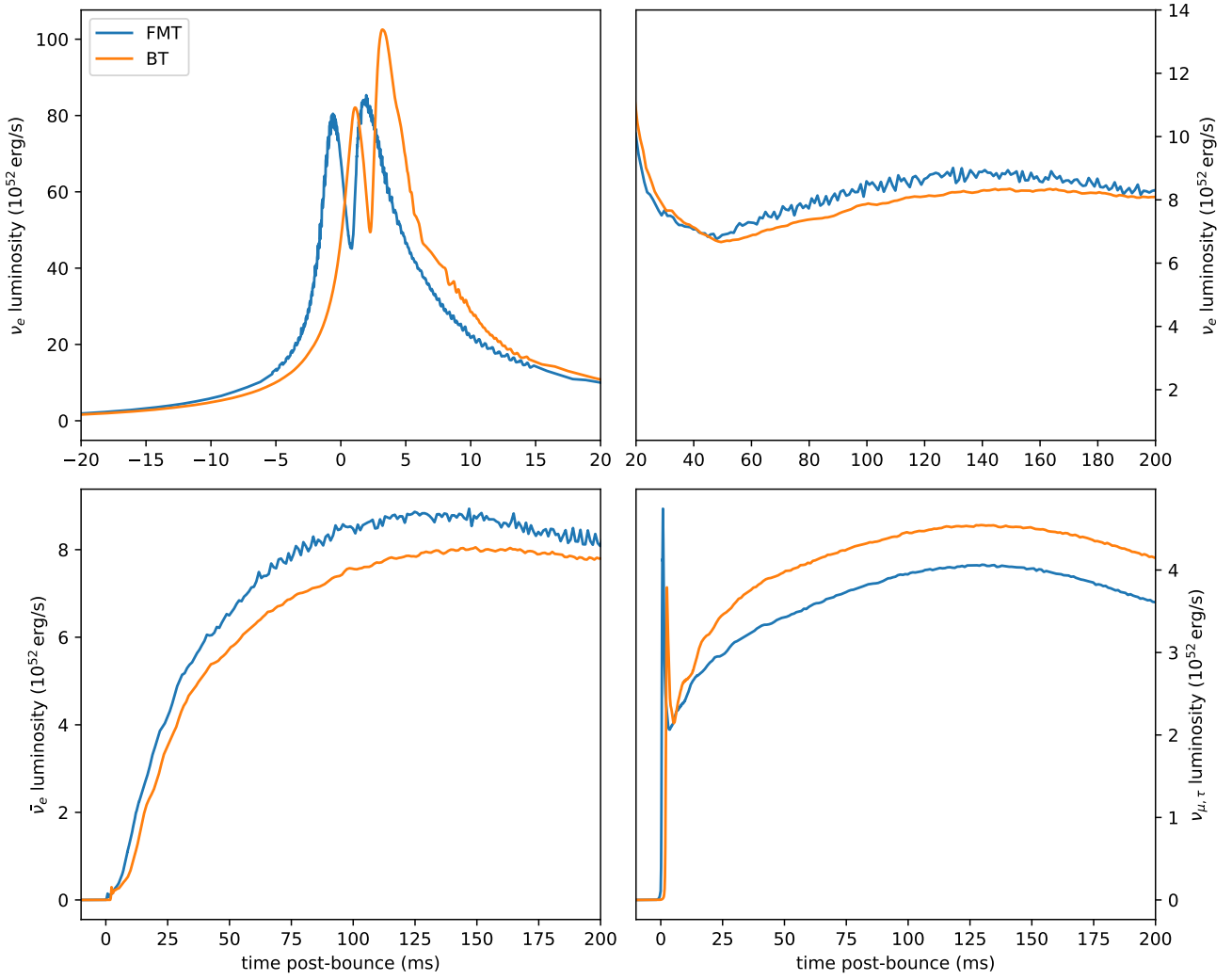


Figure 12. Neutrino luminosities for each flavor group as measured by an observer at 500 km as a function of time after bounce. We show the electron neutrino luminosity in the upper panels, with the upper left panel focusing on the neutronization burst. We show the electron antineutrino and heavy lepton neutrino luminosities in the lower left and lower right panels. Blue lines show the FMT results, and orange lines show the results from our new scheme.

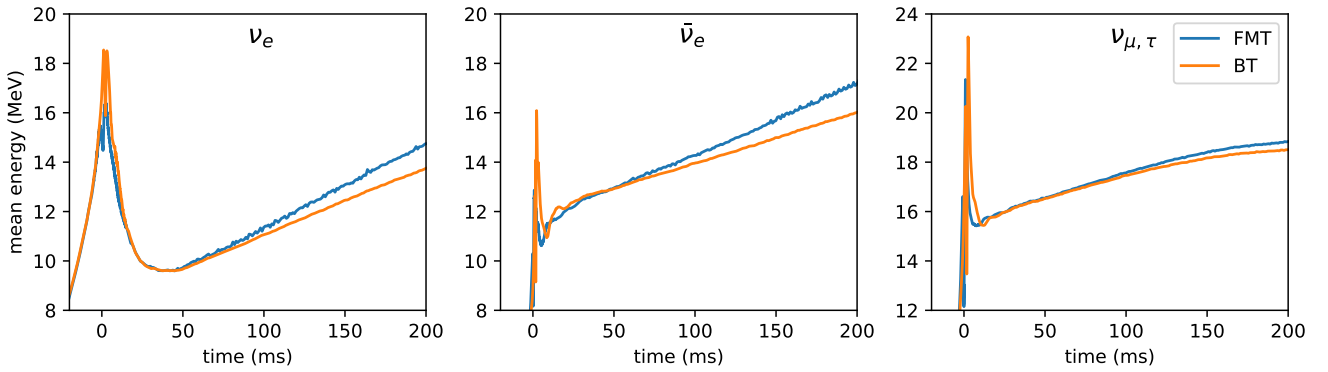


Figure 13. Mean energy of electron neutrinos, electron antineutrinos, and heavy lepton neutrinos (from left to right) as measured by an observer at 500 km as a function of time after bounce. Blue lines show the FMT results, and orange lines show the results from our new scheme.

creases once the post-shock matter becomes optically thin in FMT because a stationary transport solution is used. The electron neutrino luminosity in BT peaks at a higher value than FMT during the neutronization burst, but agrees well afterwards. One should note the rather unusual shape of the burst with a high peak luminosity and two humps of roughly equal height, which is purely due to our choice of opacities. During the accretion phase, the antineutrino luminosity is lower, whereas the heavy-lepton neutrino luminosity is higher.

In Figure (13), we show the mean neutrino energy as measured by an observer at a radius of 500 km. In BT, the mean energy peaks at roughly 2 MeV higher during the neutronization burst, but agree reasonably well afterwards. At later times, the mean energy of all three species in BT is lower. During the early post-bounce phase the differences in the luminosities and mean energies between BT and FMT are below 10%, and give a quantitative indication of the errors in the FMT scheme that stem from the transport approximation (but not from the microphysics).

Although neither run accurately maintains a constant core entropy and lepton fraction during bounce, this test sufficiently demonstrates the basic viability of our algorithm. We defer a comparison with other state-of-the-art models run using other Boltzmann transport solvers until our collisional integral has been updated to include the most recent microphysics.

Both runs were performed on the same supercomputer (OzS-TAR), providing us a means to estimate the relative computational cost. BT was run using 24 cores, while FMT was run using 1 core. The elapsed wall clock time per time step was 28 times longer in BT, which translates to 672 times more core-hours consumed. It is unsurprising that FMT is much faster, given that it is a far more approximate scheme. We emphasize, that there is a great amount of effort still need to optimize and parallelize the code before it is affordable to run in full 6D, and these timings are only rough estimates. On one hand, more expensive opacities and parallelization overheads will further increase computational cost, but on the other hand, our implementation of the algorithm is currently far from optimized.

4.5 Tests in axisymmetry

Up until now, we have performed tests in spherical symmetry, but the real advantage of our method is that it can be easily extended to two and three dimensions. We limit our tests to stationary problems in axisymmetry, which can still be computed using modest computational resources. For axisymmetric problems, periodic boundary conditions are applied in the ϕ -direction, thus we expect results to be identical on a grid in 3D with the same $\Delta\phi$.

4.5.1 Radiating sphere

We repeat the classical optically thick radiating sphere problem on the 2D grid (Figure 14). While the initial conditions are spherically symmetric, it is worthwhile performing this test in axisymmetry given that cell volumes and areas differ along the θ -direction on a spherical polar grid. We use $N_r = 100$, $N_\theta = 32$, $N_\mu = 17$, and $N_\phi = 32$.

We again find excellent agreement with the analytic solution, with a small error at the poles. Given the coordinate singularity present at the poles, this is unsurprising, and the scheme performs remarkably well despite this fact.

4.5.2 Radiating disk

Many two-moment methods have difficulty handling intersecting beams of radiation inasmuch as they produce a solution in which the beams erroneously interact. This limitation arises because the individual directions of propagation cannot be resolved with the knowledge of the moments J and H alone. To demonstrate the multi-dimensional capabilities of our code, we perform a test using very asymmetric initial conditions: a spatially thin disk radiating isotropically into a vacuum. To reproduce the correct intensity at any point above the disk, the scheme must be able to accurately handle intersecting beams. Near the surface of the disk, the flux vector is misaligned with the radial coordinate, the direction with finest angular resolution in momentum space. This poses an additional challenge to accurately resolving the transition to forward-peaked radiation.

This problem is run in the domain $0 < \theta < \frac{\pi}{2}$, with a vacuum (i.e. $\kappa_a = 0$) everywhere, and an isotropic distribution imposed along the boundary $\theta = \frac{\pi}{2}$, $-1 < r < 1$ simulating an optically thick, but geometrically thin disk with $f_{\text{eq}} = 1$. We use $N_r = 100$, $N_\theta = 32$, $N_\mu = 17$, and $N_\phi = 32$. We found that such a high resolution in angle is required to obtain an acceptable numerical solution for this particular test problem, but note that one cannot draw conclusions about resolution requirements for a less extreme problem geometry as typically encountered in core-collapse supernovae (with the exception of collapsar disks). Since the disk is optically thick, the exact solution at any point can be found by integrating the equilibrium distribution function over the projected surface of the disk

$$\mathcal{J}(x, z) = \frac{1}{4\pi} \int_0^1 \int_0^{2\pi} \frac{r z \, d\phi \, dr}{\left((x - r \cos \phi)^2 + z^2 + (r \sin \phi)^2\right)^{3/2}} \quad (86)$$

where x and z are the radius and height in *cylindrical* coordinates.

We compare the mean intensity calculated using our scheme against the exact solution at constant heights above the disk (Figure 15), and find reasonable agreement, aside from an artefact at $x = 0$ arising from the singularity of the spherical polar grid. The error is confined to the innermost three angular zones closest to the pole and could conceivably be eliminated using a range of numerical treatments. In future 3D simulations, one may resort to singularity-free grids, such as the Yin-Yang overset grid (Kageyama & Sato 2004), so the axis artefact is not a major obstacle against generalising our new algorithm to three dimensions.

5 SUMMARY AND CONCLUSIONS

Despite recent progress in developing robust and efficient approximations for neutrino transport in multi-dimensional core-collapse supernova models, simulations will ultimately have to deal with the full kinetic equations and drop the approximations inherent in diffusion and two-moment closure schemes. In this paper, we have introduced a new, locally implicit scheme for solving the full general relativistic Boltzmann transport equation in the context of neutrino transport in core-collapse supernovae.

Our scheme uses the discrete-ordinate method to discretise the six-dimensional phase space into volume elements. We eliminate the need to implement angle and energy derivatives associated with geometric rotations and relativistic effects by using a semi-Lagrangian interpolation method to account for the frame transformations between adjacent cells. The propagation of neutrinos in a relativistic spacetime is taken care of by applying appropriate

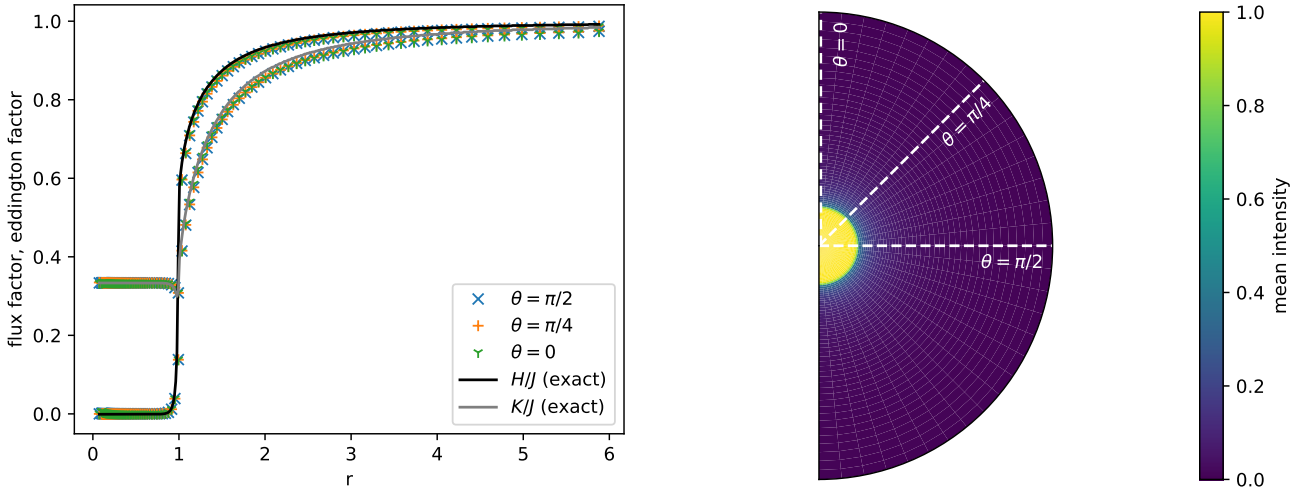


Figure 14. Left: Flux factor and Eddington factor along 3 rays (crosses) compared to the exact solutions (lines). The numerical solution along each ray is nearly identical, as expected. Right: Dashed lines the rays where the numerical solution is compared to the exact solution.

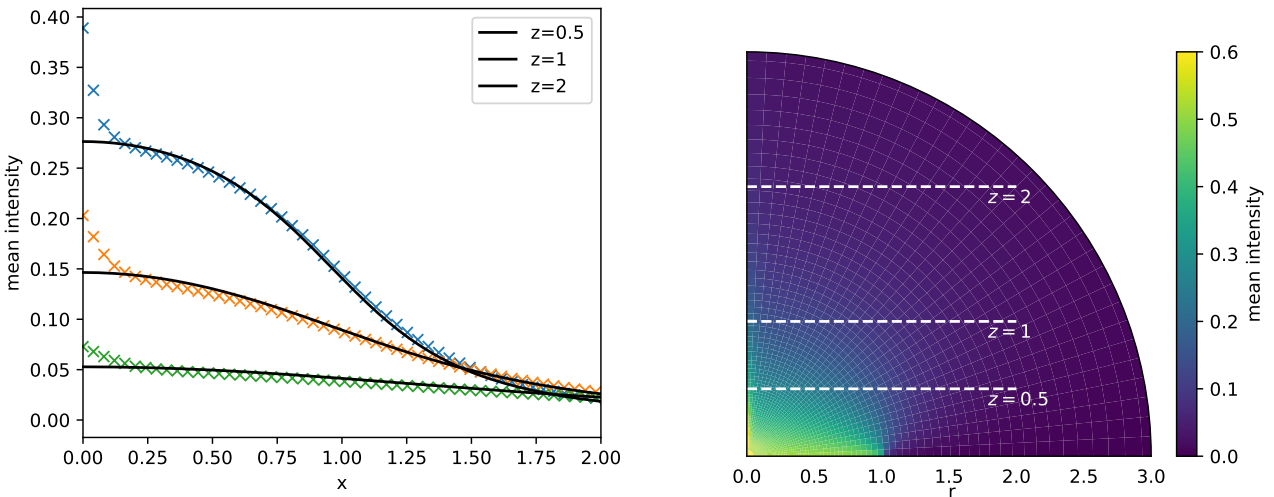


Figure 15. Left: Mean intensity as a function of distance from the center at three heights above the disk calculated using our scheme (crosses), compared to the exact solution (line). Right: Dashed lines indicate heights at which the intensity is compared to the exact solution.

Hamiltonian “kicks” to advected neutrinos. Although the algorithm can accommodate arbitrary spacetime metrics, we limit ourselves to a conformally flat metric (Isenberg 2008; Wilson et al. 1996; Cordero-Carrion et al. 2009) in our current work. The scheme guarantees neutrino number conservation by construction, and also has very good energy conservation properties. Neutrino fluxes between cells are computed using a semi-implicit Lax-Wendroff discretisation of the Boltzmann equation, which is consistent with the diffusion limit. In our scheme, we discretise the collision integral implicitly to maintain stability. By discretising the advection terms explicitly, we avoid a global coupling in space, which obviates the need for a complicated infrastructure for global iterative solves of huge non-linear systems, and makes parallel scaling of massive simulations easier. The simplicity of the algorithm and the purely local treatment of the collision integral will also facilitate future extensions to the code (e.g., additional interaction processes, generalisation to the quantum kinetic equations).

We have shown, using a suite of analytically solvable tests in spherical symmetry, that our scheme is accurate both in the diffusive regime and the free-streaming regimes. We have also shown using tests in axisymmetry that our scheme is equally applicable in 2D, and argue that it will extend easily to 3D. We have demonstrated that our scheme, when coupled to the general relativistic hydrodynamics solver CoCoNuT, can be used to model the collapse and accretion phase of core-collapse supernovae in spherical symmetry. Currently, the coupled neutrino hydrodynamics code uses a reduced set of neutrino interactions. We have not yet included non-isoeenergetic scattering (NIS) in our collision integral, which critically affects the dynamics of the collapse phase (Bruenn 1985; Mezzacappa & Bruenn 1993c), treat Bremsstrahlung as a one-particle reaction, and omit the pair process and neutrino pair conversion (Buras et al. 2003). The collapse test also revealed some residual problems with entropy and lepton fraction advection errors in the innermost zones during the end of the collapse phase, which

can likely be fixed using a more careful treatment of the origin of the spherical polar grid. A more detailed comparison with other neutrino transport codes in the vein of [Liebendörfer et al. \(2005\)](#); [Müller et al. \(2012\)](#); [Richers et al. \(2017\)](#); [O'Connor et al. \(2018\)](#); [Just et al. \(2018\)](#) will be carried out once the required microphysics is in place.

Computer time requirements for our algorithm will increase significantly once the collision integral is treated in its most general form. In order to maximise the accuracy and efficiency of our new Boltzmann scheme and facilitate its application in multi-dimensional supernova simulations, one can consider a number of improvements to the algorithm. A disadvantage of discrete ordinate schemes is that they require high angular resolution to resolve the distribution as $\mu \rightarrow 1$ in the free-streaming limit. Although our scheme already performs quite well because we have used $\mu = 1$ as a collocation point, our mapping method lends itself to easy implementation of an adaptive grid in momentum space proposed by [Yamada et al. \(1999\)](#). In practice, however, this may yield only a minimal improvement in core-collapse models, since the forward-peaked regions are far outside the region of dynamical influence, but an adaptive grid in angle and/or energy might allow us to achieve comparable results with significantly lower resolution in momentum space.

More substantial savings may be gained by introducing local timestepping. In our implementation, we have used global timesteps, which are limited by the small zones at the center of the grid. Since the timestep can be much larger in the larger outer zones, a local timestepping method may provide computational cost savings. Furthermore, the timestep can be increased above the CFL limit in diffusive zones without compromising stability. We will also explore numerical techniques to optimise the implicit solution of the neutrino source terms for complicated interaction kernels.

A major uncertainty in the treatment of neutrinos in core-collapse supernovae comes from the effects of neutrino flavour conversion. While the classical Mikheyev-Smirnov-Wolfenstein (MSW) effect ([Wolfenstein 1978](#); [Mikheyev & Smirnov 1985](#)) is significant at densities of 10^0 - 10^3 g/cm³, and only influences the observed neutrino signal rather than the dynamics in the supernova core, flavour conversion due to ν - ν interactions (e.g. [Pantaleone 1992](#); [Duan et al. 2010](#); [Mirizzi et al. 2016](#)) may occur deeper in the core and have tangible repercussions on the dynamics of the pre-explosion and explosion phase, and on supernova nucleosynthesis. In particular, multi-angle effects (e.g. [Sawyer 2005, 2009](#); [Cherry et al. 2012](#); [Dasgupta et al. 2017](#)) could result in fast flavour conversion already in the region of the neutrinosphere. Flavour conversion cannot be consistently implemented in supernova simulations yet.⁸

Since the detailed angular distribution of neutrinos can be critical in the flavour conversion problem, and since the validity of closure approximations in the quantum kinetic regime is doubtful, a multi-dimensional Boltzmann treatment is an essential stepping stone towards a consistent inclusion of flavour conversion in supernova simulations in the long term. Incorporating flavour conversion will entail replacing the (flavour-dependent) distribution function with a density matrix that obeys the equations of quantum kinetic theory (e.g. [Sigl & Raffelt 1993](#); [Cardall 2008](#); [Volpe 2015](#); [Richers](#)

⁸ There are first ideas to use solvers for the quantum kinetic equations for more than post-processing ([Stapleford et al. 2019](#)), but these are not fully convincing and far from achieving a consistent coupling of the hydrodynamics with the quantum kinetic equations

[et al. 2019](#)). Although considerable work is still needed to understand the complicated instabilities in the non-linear flavor conversion problem, our scheme provides a suitable framework for implementing the relevant macroscopic equations. While a consistent treatment of flavour conversion in supernovae is not yet on the horizon and will require prodigious interdisciplinary efforts, we believe there may be considerable use for a conceptually simple, locally implicit algorithm for neutrino kinetics as outlined in this paper.

ACKNOWLEDGEMENTS

We thank Alexander Heger for useful discussions. CC was supported by an Australian Government Research Training Program (RTP) Scholarship. This work was supported by the Australian Research Council through ARC Future Fellowship FT160100035. We acknowledge CPU time on OzSTAR funded by Swinburne University and the Australian Government. This research was undertaken with the assistance of resources obtained via NCMAS and ASTAC from the National Computational Infrastructure (NCI), which is supported by the Australian Government and was supported by resources provided by the Pawsey Supercomputing Centre with funding from the Australian Government and the Government of Western Australia.

APPENDIX A: INTERFACE FLUXES IN THE DIFFUSION LIMIT

The distribution function can be expressed as an expansion of its moments

$$f = \mathcal{J} + \mu\mathcal{H} + \dots \quad (\text{A1})$$

to solve the Boltzmann equation, which can be expressed in planar geometry as

$$\frac{\partial f}{\partial t} + \mu \frac{\partial f}{\partial z} = \kappa_a (\mathcal{J}_{\text{eq}} - f) + \kappa_s (\mathcal{J} - f). \quad (\text{A2})$$

The equation for the first moment becomes

$$\frac{\partial \mathcal{H}}{\partial t} + \frac{\partial \mathcal{K}}{\partial z} = -(\kappa_a + \kappa_s) \mathcal{H}. \quad (\text{A3})$$

In the diffusion limit, $\frac{\partial \mathcal{H}}{\partial t} \rightarrow 0$, thus we obtain

$$\mathcal{H} = -\frac{1}{\kappa_a + \kappa_s} \frac{\partial \mathcal{K}}{\partial z}. \quad (\text{A4})$$

We seek a discretisation of the Boltzmann equation that approaches the same limit of \mathcal{H} for the numerical fluxes. In the Lax-Wendroff scheme, the fluxes at the interface between i and $i+1$, labelled $i+\frac{1}{2}$, for a particular direction μ_j , are

$$f_{i+\frac{1}{2}}^{n+\frac{1}{2}} = f_{i+\frac{1}{2}}^n + \frac{\Delta t}{2} \left(\mu_j \frac{f_i^n - f_{i+1}^n}{\Delta z} \right) + \frac{\Delta t}{2} \kappa_a \left(\mathcal{J}_{\text{eq}} - f_{i+\frac{1}{2}}^{n+\frac{1}{2}} \right) + \frac{\Delta t}{2} \kappa_s \left(\mathcal{J} - f_{i+\frac{1}{2}}^{n+\frac{1}{2}} \right). \quad (\text{A5})$$

For optically thick cells, $\frac{\Delta t}{2} (\kappa_a + \kappa_s) \gg 1$, thus

$$\mu \frac{f_i^n - f_{i+1}^n}{\Delta z} = \kappa_a \left(\mathcal{J}_{\text{eq}} - f_{i+\frac{1}{2}}^{n+\frac{1}{2}} \right) + \kappa_s \left(\mathcal{J} - f_{i+\frac{1}{2}}^{n+\frac{1}{2}} \right). \quad (\text{A6})$$

Multiplying by μ , integrating over all directions j , and simplifying gives

$$\frac{\sum_j \mu_j^2 f_{i+1}^n \Delta\mu_j - \sum_j \mu_j^2 f_i^n \Delta\mu_j}{\Delta z} = -(\kappa_a + \kappa_s) \times \sum_j \mu_j f_{i+\frac{1}{2}}^{n+\frac{1}{2}} \Delta\mu_j \quad (\text{A7})$$

$$\frac{\Delta \mathcal{K}_{i+\frac{1}{2}}^n}{\Delta z} = -(\kappa_a + \kappa_s) \mathcal{H}_{i+\frac{1}{2}}^{n+\frac{1}{2}}, \quad (\text{A8})$$

which is the discretised form of Equation (A4) at cell interfaces.

REFERENCES

- Abdikamalov E., Burrows A., Ott C. D., Löffler F., O'Connor E., Dolence J. C., Schnetter E., 2012, *ApJ*, 755, 111
- Arnett W. D., 1977, *ApJ*, 218, 815
- Arnett W. D., Truran J. W., 1970, *ApJ*, 160, 959
- Ascher U. M., Ruuth S. J., Spiteri R. J., 1997, *Applied Numerical Mathematics*, 25, 151
- Audit E., Charrier P., Chièze J. P., Dubroca B., 2002, arXiv e-prints, pp astro-ph/0206281
- Baron E., Myra E. S., Cooperstein J., van den Horn L. J., 1989, *ApJ*, 339, 978
- Bowers R. L., Wilson J. R., 1982, *ApJS*, 50, 115
- Boyd J. P., 2000, *Chebyshev and Fourier Spectral Methods: Second Revised Edition*. Dover Publications
- Bruenn S. W., 1985, *ApJS*, 58, 771
- Bruenn S. W., et al., 2018, arXiv e-prints, p. arXiv:1809.05608
- Buras R., Janka H.-T., Keil M. T., Raffelt G. G., Rampp M., 2003, *ApJ*, 587, 320
- Buras R., Janka H. T., Rampp M., Kifonidis K., 2006, *A&A*, 457, 281
- Burrows A., 2013, *Reviews of Modern Physics*, 85, 245
- Burrows A., Hayes J., Fryxell B. A., 1995, *ApJ*, 450, 830
- Burrows A., Young T., Pinto P., Eastman R., Thompson T. A., 2000, *ApJ*, 539, 865
- Burrows A., Dessart L., Livne E., Ott C. D., Murphy J., 2007, *ApJ*, 664, 416
- Cardall C. Y., 2008, *Phys. Rev. D*, 78, 085017
- Cardall C. Y., Endeve E., Mezzacappa A., 2013, *Phys. Rev. D*, 88, 023011
- Carlson B. G., 1967, *Computational Methods in Physics*, Vol. 1. Academic Press
- Cherry J. F., Carlson J., Friedland A., Fuller G. M., Vlasenko A., 2012, *Phys. Rev. Lett.*, 108, 261104
- Chu R., Endeve E., Hauck C. D., Mezzacappa A., 2019, *Journal of Computational Physics*, 389, 62
- Colgate S. A., White R. H., 1966, *ApJ*, 143, 626
- Cooperstein J., Baron E., 1992, *ApJ*, 398, 531
- Cordero-Carrion I., Cerdá-Durán P., Dimmelmeier H., Jaramillo J. L., Novak J., Gourgoulhon E., 2009, *Phys. Rev. D*, 79, 024017
- Dasgupta B., Mirizzi A., Sen M., 2017, *J. Cosmology Astropart. Phys.*, 2017, 019
- Dimmelmeier H., Novak J., Font J. A., Ibáñez J. M., Müller E., 2005, *Phys. Rev. D*, 71, 064023
- Duan H., Fuller G. M., Qian Y.-Z., 2010, *Annual Review of Nuclear and Particle Science*, 60, 569
- Fleck J. A. J., Canfield E. H., 1984, *Journal of Computational Physics*, 54, 508
- Fleck J. A. J., Cummings J. D., 1971, *Journal of Computational Physics*, 8, 313
- Foucart F., 2018, *MNRAS*, 475, 4186
- Fryer C. L., Heger A., 2000, *ApJ*, 541, 1033
- Fryer C. L., Warren M. S., 2004, *ApJ*, 601, 391
- Glas R., Just O., Janka H. T., Obergaulinger M., 2019, *ApJ*, 873, 45
- González M., Audit E., Huynh P., 2007, *A&A*, 464, 429
- Herant M., Benz W., Hix W. R., Fryer C. L., Colgate S. A., 1994, *ApJ*, 435, 339
- Hubeny I., Burrows A., 2007, *ApJ*, 659, 1458
- Isenberg J. A., 2008, *International Journal of Modern Physics D*, 17, 265
- Janka H. T., 1992, *A&A*, 256, 452
- Janka H.-T., 2012, *Annual Review of Nuclear and Particle Science*, 62, 407
- Janka H. T., Hillebrandt W., 1989, *A&AS*, 78, 375
- Just O., Obergaulinger M., Janka H. T., 2015, *MNRAS*, 453, 3386
- Just O., Bollig R., Janka H. T., Obergaulinger M., Glas R., Nagataki S., 2018, *MNRAS*, 481, 4786
- Kageyama A., Sato T., 2004, *Geochemistry, Geophysics, Geosystems*, 5, Q09005
- Kuroda T., Takiwaki T., Kotake K., 2016, *ApJS*, 222, 20
- Levermore C. D., 1984, *J. Quant. Spectrosc. Radiative Transfer*, 31, 149
- Liebdörfer M., Mezzacappa A., Thielemann F.-K., Messer O. E., Hix W. R., Bruenn S. W., 2001, *Phys. Rev. D*, 63, 103004
- Liebdörfer M., Messer O. E. B., Mezzacappa A., Bruenn S. W., Cardall C. Y., Thielemann F. K., 2004, *ApJS*, 150, 263
- Liebdörfer M., Rampp M., Janka H. T., Mezzacappa A., 2005, *ApJ*, 620, 840
- Liebdörfer M., Whitehouse S. C., Fischer T., 2009, *ApJ*, 698, 1174
- Livne E., Burrows A., Walder R., Lichtenstadt I., Thompson T. A., 2004, *ApJ*, 609, 277
- Marek A., Dimmelmeier H., Janka H. T., Müller E., Buras R., 2006, *A&A*, 445, 273
- Mezzacappa A., 2005, *Annual Review of Nuclear and Particle Science*, 55, 467
- Mezzacappa A., Bruenn S. W., 1993a, *ApJ*, 405, 637
- Mezzacappa A., Bruenn S. W., 1993b, *ApJ*, 405, 669
- Mezzacappa A., Bruenn S. W., 1993c, *ApJ*, 410, 740
- Mezzacappa A., Liebdörfer M., Messer O. E., Hix W. R., Thielemann F.-K., Bruenn S. W., 2001, *Phys. Rev. Lett.*, 86, 1935
- Mihalas D., Mihalas B. W., 1984, *Foundations of radiation hydrodynamics*. Oxford University Press, New York
- Mikheyev S. P., Smirnov A. Y., 1985, *Yadernaya Fizika*, 42, 1441
- Minerbo G. N., 1978, *J. Quant. Spectrosc. Radiative Transfer*, 20, 541
- Mirizzi A., Tamborra I., Janka H. T., Saviano N., Scholberg K., Bollig R., Hüdepohl L., Chakraborty S., 2016, *Nuovo Cimento Rivista Serie*, 39, 1
- Misner C. W., Thorne K. S., Wheeler J. A., 1973, *Gravitation*. W.H. Freeman and Co., San Francisco
- Müller B., Janka H. T., 2015, *MNRAS*, 448, 2141
- Müller B., Janka H.-T., Dimmelmeier H., 2010, *ApJS*, 189, 104
- Müller B., Janka H.-T., Marek A., 2012, *ApJ*, 756, 84
- Murchikova E. M., Abdikamalov E., Urbatsch T., 2017, *MNRAS*, 469, 1725
- Myra E. S., Bludman S. A., Hoffman Y., Lichtenstadt I., Sack N., van Riper K. A., 1987, *ApJ*, 318, 744
- Nagakura H., Sumiyoshi K., Yamada S., 2014, *ApJS*, 214, 16
- O'Connor E., 2015, *ApJS*, 219, 24
- O'Connor E., et al., 2018, *Journal of Physics G Nuclear Physics*, 45, 104001
- Ott C. D., Burrows A., Dessart L., Livne E., 2008, *ApJ*, 685, 1069
- Pantaleone J., 1992, *Physics Letters B*, 287, 128
- Peres B., Penner A. J., Novak J., Bonazzola S., 2014, *Classical and Quantum Gravity*, 31, 045012
- Pons J. A., Reddy S., Prakash M., Lattimer J. M., Miralles J. A., 1999, *ApJ*, 513, 780
- Pons J. A., Ibáñez J. M., Miralles J. A., 2000, *MNRAS*, 317, 550
- Radice D., Abdikamalov E., Rezzolla L., Ott C. D., 2013, *Journal of Computational Physics*, 242, 648
- Rahman N., Just O., Janka H. T., 2019, *MNRAS*, 490, 3545
- Rampp M., Janka H. T., 2000, *ApJ*, 539, L33
- Rampp M., Janka H. T., 2002, *A&A*, 396, 361
- Richers S., Nagakura H., Ott C. D., Dolence J., Sumiyoshi K., Yamada S., 2017, *ApJ*, 847, 133
- Richers S. A., McLaughlin G. C., Kneller J. P., Vlasenko A., 2019, *Phys. Rev. D*, 99, 123014
- Roberts L. F., Ott C. D., Haas R., O'Connor E. P., Diener P., Schnetter E., 2016, *ApJ*, 831, 98
- Ryan B. R., Dolence J. C., 2020, *ApJ*, 891, 118
- Sawyer R. F., 2005, *Phys. Rev. D*, 72, 045003
- Sawyer R. F., 2009, *Phys. Rev. D*, 79, 105003

- Sigl G., Raffelt G., 1993, *Nuclear Physics B*, 406, 423
- Skinner M. A., Burrows A., Dolence J. C., 2016, *ApJ*, 831, 81
- Skinner M. A., Dolence J. C., Burrows A., Radice D., Vartanyan D., 2019, *ApJS*, 241, 7
- Smit J. M., Cernohorsky J., Dullemond C. P., 1997, *A&A*, 325, 203
- Stapleford C. J., Fröhlich C., Kneller J. P., 2019, arXiv e-prints, p. arXiv:1910.04172
- Sumiyoshi K., Yamada S., 2012, *ApJS*, 199, 17
- Swesty F. D., Myra E. S., 2009, *ApJS*, 181, 1
- Tolman R. C., Ehrenfest P., 1930, *Physical Review*, 36, 1791
- Volpe C., 2015, *International Journal of Modern Physics E*, 24, 1541009
- Walder R., Burrows A., Ott C. D., Livne E., Lichtenstadt I., Jarrar M., 2005, *ApJ*, 626, 317
- Wilson J. R., Mathews G. J., Marronetti P., 1996, *Phys. Rev. D*, 54, 1317
- Wolfenstein L., 1978, *Phys. Rev. D*, 17, 2369
- Yamada S., Janka H.-T., Suzuki H., 1999, *A&A*, 344, 533
- Yueh W. R., Buchler J. R., 1977, *ApJ*, 217, 565
- larsen E. W., Morel J. E., 1989, *Journal of Computational Physics*, 83, 212
- van Leer B., 1977, *Journal of Computational Physics*, 23, 276